

CERN – EUROPEAN ORGANIZATION FOR NUCLEAR RESEARCH



CLIC – Note – 1061

**DEVELOPMENT OF X-BAND HIGH-POWER RF LOAD FOR CLIC
APPLICATIONS USING ADDITIVE MANUFACTURING TECHNIQUES.**

Gian Luigi D'Alessandro

European Organization for Nuclear Research, Geneva, Switzerland &
University of Salento, Lecce, Italy

CERN-THESIS-2015-315
30/10/2015



Geneva, Switzerland
14.12.2015

European Organization for Nuclear Research & University of Salento,
Mathematics and Physics Department.

Development of X-band High-Power RF load for CLIC applications
using additive manufacturing techniques.

A thesis submitted in satisfaction of the requirements for the degree Bachelors
of Science in Physics by Gian Luigi D'Alessandro

First Reviewer: Alexej Grudiev

Second Reviewer: Walter Wuensch

Geneva 26.11.2015

This page intentionally left blank

Table of contents

List of tables	6
List of figures	7
Executive summary	11

Chapter 1

Introduction

1.1 CLIC structure	15
--------------------	----

Chapter 2

Waveguides and Reflection

2.1 Theory of Propagation in Waveguides	18
2.2 Rectangular Waveguide	21
2.3 Scattering Parameters	25

Chapter 3

Simple Load Model

3.1 Application of the concepts to rectangular waveguides	29
3.2 Simple Load Model	34

Chapter 4

New Concept Load

4.1 Geometry Description	39
4.2 Vacuum pumping holes	44
4.3 Input Box	48

4.4 Considerations	52
--------------------	----

Chapter 5

Thermal Simulations

5.1 Power	54
5.2 Model for Simulations	57
5.3 Heat Transfer Theory	59
5.4 Applications of Heat Transfer Theory	62
5.5 Pressure	71

Chapter 6

RF Check

6.1 CATIA model	74
-----------------	----

Conclusions	77
--------------------	----

Appendixes

A 3D Printing Technologies	78
B Ti6Al4V alloy	80

References	82
-------------------	----

Acknowledgments	85
------------------------	----

This page intentionally left blank

List of tables

Tables Chapter 3

Table 3A. S_{12} parameter narrow waveguide.

Table 3B. S_{12} parameter WR90 waveguide.

Table 3C. S_{12} parameter tapered waveguide.

Tables Chapter 4

Table 4A. List of radii for linear-growing spiral

Table 4B. List of radii for non-linear-growing spiral

Tables Chapter 5

Table 5A. Specifics of Klystron and AS

Table 5B. List of convection coefficient for the cooling system.

Table 5C. Temperature values for 15217 ($W/(m^2)C$) heat coefficient.

Table 5D. Deformation values for 15217 ($W/(m^2)C$) heat coefficient.

Table 5E. Stress values for 15217 ($W/(m^2)C$) heat coefficient.

Table 5F. List of pressure drops in function of velocities for the cooling system.

Table Appendix B

Table B. Ti6Al4V Specifics

List of Figures

Figures Executive Summary

Figure1. CLIC accelerator scheme.

Figure2. Schematic layout of CLIC Type-0 module

Figure3. Schematic layout of CLIC modules with different Main Beam quadrupoles

Figure4. 3D view of a Type-1 CLIC two-beam module

Figures Chapter 1

Figure1.1. Schematic view of the CLIC module RF system

Figure1.2. 3D model of the choke mode flange, hybrid and load

Figure1.3. Schematic view of the CLIC 'dry' RF load

Figure1.4. Old-generation load

Figures Chapter 2

Figure2.1.1. Coaxial transmission line for cylindrical pipe.

Figure 2.2.1. Rectangular waveguide.

Figure 2.2.2. Electric field distribution for the first three TE_{n0} modes in a rectangular waveguide.

Figure2.3.1. 2-port network.

Figures Chapter 3

Figure3.1.1 S_{12} parameter plot narrow waveguide

Figure3.1.2. S_{12} parameter plot WR90 waveguide

Figure3.1.3. TE_{10} mode in WR90 waveguide.

Figure3.1.4. Tapered waveguide

Figure3.1.5. S_{12} values plot tapered waveguide

Figure3.1.6. S_{12} values comparison plot for three waveguides

Figure3.2.1. Scattering parameters for a load and related waveguide

Figure3.2.2. S_{11} parameter plot tapered load HFSS

Figure3.2.3. Average Roughness.

Figure3.2.4. S_{11} parameter plot tapered load HFSS, Roughness

Figures Chapter 4

Figure 4.1.1. Spiral polyline, on the left.

Figure 4.1.2. Spiral walls.

Figure 4.1.3. Spiral after subtraction, vacuum model.

Figure4.1.4. S_{11} values plot for spiral load HFSS, with and without Roughness

Figure4.1.5. S_{11} values comparison between spiral and tapered load, HFSS, Roughness

Figure 4.2.1 Spiral with holes top-view

Figure 4.2.2 Spiral with holes side-view

Figure 4.2.3. Spiral with holes.

Figure 4.2.4. Spiral with holes detail zooming after rounding

Figure4.2.5. S_{11} parameter plot, spiral load with holes HFSS, with and without Roughness

Figure4.2.6. S_{11} parameter comparison between three previous models, no Roughness

Figure4.2.7. S_{11} values comparison between three previous models, Roughness

Figure4.3.1. Input waveguide.

Figure4.3.2. S_{11} parameter for different lengths of the input.

Figure4.3.3. Spiral with input side-view.

Figure4.3.4. S_{11} parameter plot spiral load with input, with and without Roughness

Figure4.3.5. S_{11} parameter comparison plot for Spiral with holes and spiral with input, no Roughness

Figure4.3.6. S_{11} parameter comparison plot for Spiral with holes and spiral with input, Roughness

Figures Chapter 5

Figure5.1.1. Power loss density (W/m^2).

Figure5.1.2. Klystron on the left, Klystron scheme on the right.

Figure5.1.3. AS on the left, AS scheme on the right

Figure5.1.4. Average Power

Figure5.1.5. Metal model

Figure5.1.6. Cooling system, symmetric cut in the zy plane.

Figure5.1.7. Load with cooling system.

Figure5.2.1. Laminar and turbulent flow.

Figure5.2.2. Flow on a plate.

Figure5.3.1. Convection coefficient of the cooling system in function of velocity.

Figure5.3.2. Temperature field of the load.

Figure5.3.3. Temperature field of the load, cut in xy plane

Figure5.3.4. ΔT in function of input Power for different h coefficients.

Figure5.3.5. Deformation field of the load

Figure5.3.6. Deformation field of the load, cut in xy plane

Figure5.3.7. Stress field of the load.

Figure5.3.8. Stress field of the load, xy plane cut.

Figure5.3.9. ΔS in function of input Power for different h coefficients.

Figure5.4.1. Pressure drop in function of velocity on logarithmic scale

Figure Chapter 6

Figure 6.1.1. CATIA model of the load

Figure 6.1.2. CATIA model internal part

Figure 6.1.3. RF check

Figures Appendix A

FigureA.1.Laser sintering 3D printer

FigureA.2.Electron beam 3D printer

Figure Appendix B

FigureB.1.Race car gear-box fabricated with Ti6Al4V

This page intentionally left blank

Executive Summary

CLIC. Following the successful development and operation of the 100 GeV SLAC Linear Collider (SLC)[1]. The Compact Linear Collider (CLIC)[2] study is exploring the possibility of extending the energy range of linear colliders into the multi-TeV energy region by developing a novel technology of two-beam acceleration (TBA).

CLIC structure. Taking into account preliminary physics studies based on an electron–positron collider in the multi-TeV energy range [3], [4], CLIC study is focused on the design of a collider with a centre-of-mass collision energy of 3 TeV and a luminosity of $2 \times 10^{34} \text{ cm}^{-2} \text{ s}^{-1}$; these numbers being the extreme of the considered parameter space. Before describing the layout of the accelerator complex, the main design arguments and the choices that make up the so-called ‘CLIC technology’ are listed.

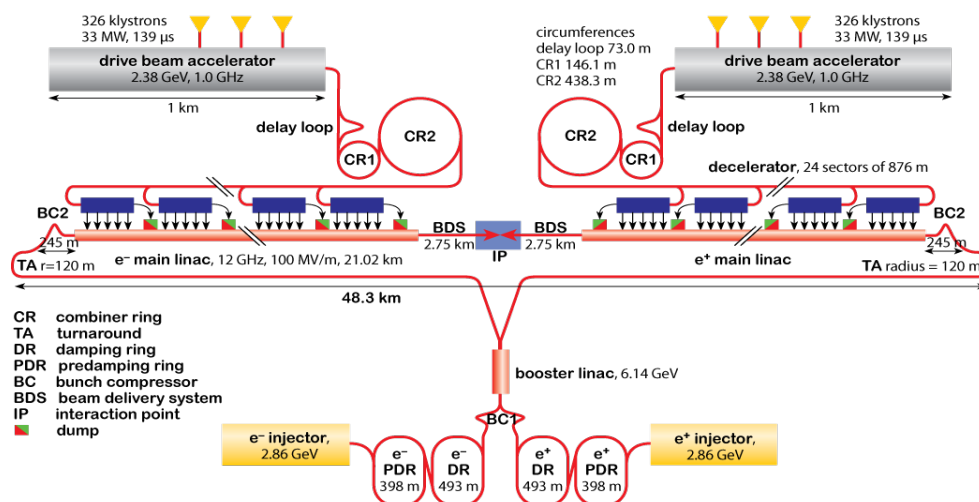


Figure 1. Layout of the CLIC accelerator complex .

The layout of the CLIC accelerator complex is shown in Fig.1. The Main Beams are generated and pre-accelerated in the injector linacs and then enter the Damping Rings for emittance reduction (lower part of the figure). Target figures are 500 nm and 5 nm normalized beam emittances in the horizontal and vertical planes respectively at the exit of the injector complex.

The small emittance beams are further accelerated in a common Linac before being transported through the main tunnel to the turnarounds. After the turnarounds the acceleration of the Main Beam begins with an accelerating gradient of 100 MV/m. Using a classic approach the Linacs for the acceleration of the Main Beams would be powered by klystrons. In this novel acceleration scheme the klystron powering is replaced by the generation of a second ‘Drive Beam’ and its compression and reversion into RF power close to the Main Beam accelerating structures.

The top part of the figure shows the Drive Beam generation in two Main Linacs and the successive time compression of the Drive Beam pulses in the Delay Loops and Combiner Rings (CR1 and CR2). The time-compressed Drive Beam reaches a current of about 100A at a beam energy of about 2.4 GeV. This compressed Drive Beam is transported through the

Main Linac tunnel to 24 individual turnarounds. Each Drive Beam segment is directed by pulsed extraction elements, for the final RF power generation, into the accelerating structures of the Main Beams. Hence in the Main Linac tunnel we find four beam transport lines: the transport lines of the Main Beam and Drive Beam plus the acceleration line for the Main Beam and the deceleration line for the Drive Beam. The beams collide after a long Beam Delivery

Section (BDS) (collimation, final focus) in one interaction point (IP) in the centre of the complex [5],[6]R.

Two-beam configuration. The CLIC two-beam configuration along most of the length of the Main and Drive linacs consists of 'repeated modules' [7] and [8]. Each Main Linac contains more than 10 000 such modules. The Drive Beam generates in each of the Power Extraction and Transfer Structures (PETS) the RF power for two accelerating structures. Each module contains up to four PETS (see Fig.2). Space for quadrupoles in the main linac is made by leaving out two, four, six, or eight accelerating structures and suppressing the corresponding PETS (see Fig.3).

In order to accommodate all needed configurations five types of modules are needed. Type-0 modules contain only accelerating structures in the Main Beam line whereas Type-1 to Type-4 modules have Main Beam Quadrupoles (MBQs) of variable length, replacing 2, 4, 6 or 8 accelerating structures correspondingly .

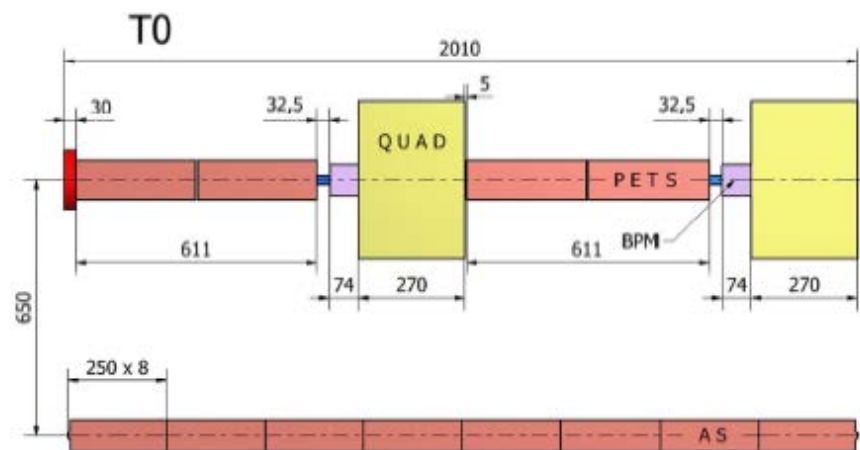


Figure2. Schematic layout of CLIC Type-0 module

Module. The module components are mounted on alignment girders. The module length is determined mainly by considerations about the mechanical and thermal stability of the overall system. Presently a value of 2010 is chosen. Drive Beam linac simulations show that the Drive Beam Quadrupole spacing must be about 1m with a quadrupole length of about 270mm to produce sufficient strength. The remaining space is available for two PETS and the BPM. A length of 30mm has been reserved for inter-girder connections. A few modules with only Main Beam and Drive Beam quadrupoles are needed where each Drive Beam is fed into and out of a Drive Beam linac sector.

The two-beam module design has to take into consideration the requirements for the different technical systems. The main components are designed and integrated to optimize the filling factor and gain in compactness. Fig.4, shows a 3D view of a typical two-beam module, with the main components, such as accelerating structures, PETS and quadrupoles. In the following subsections all main technical systems are described.

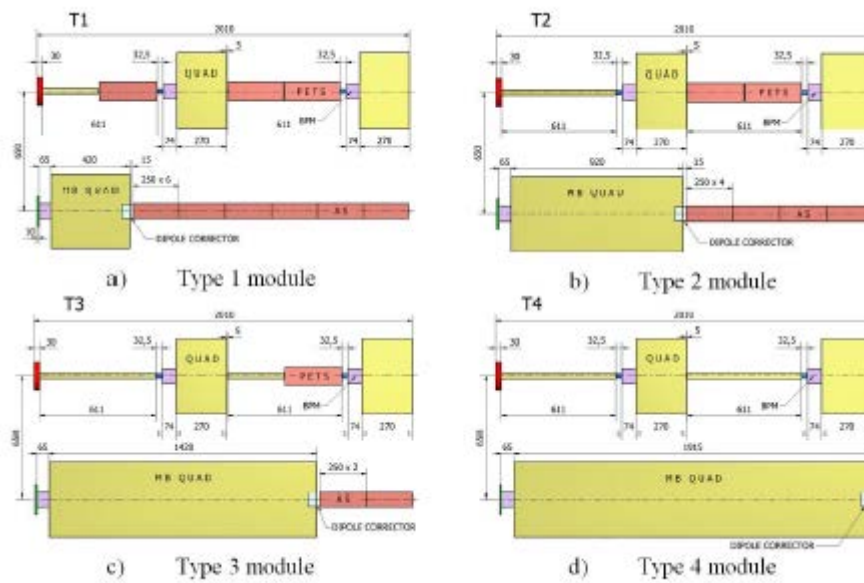


Figure 3. Schematic layout of CLIC modules with different Main Beam quadrupoles

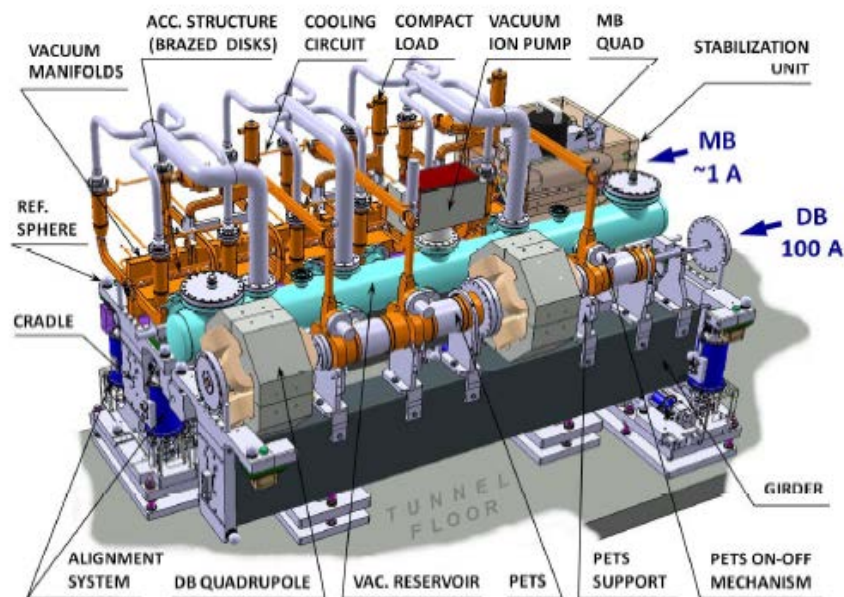


Figure 4. 3D view of a Type-1 CLIC two-beam module, we can notice the compact load up in the centre.

Without giving more details about all the module components it is worth to point out the component called ‘compact load’ see Fig.4. This component is the subject of this document and will be described furtherly in Chapter 1.

This page intentionally left blank

Chapter 1

Introduction

1.1 CLIC structures

RF network. The CLIC two-beam RF network, starting from the PETS compact coupler, includes all the RF components needed for the power extraction and distribution from PETS to “ACS”, accelerating structure, (as well as terminating the output of ACS, such as standard X-band rectangular WR-90 waveguides, hybrids, and the loads. Fig. 1.1 and 1.2 illustrate the layout of the RF system and the RF network near the accelerating structure inputs.

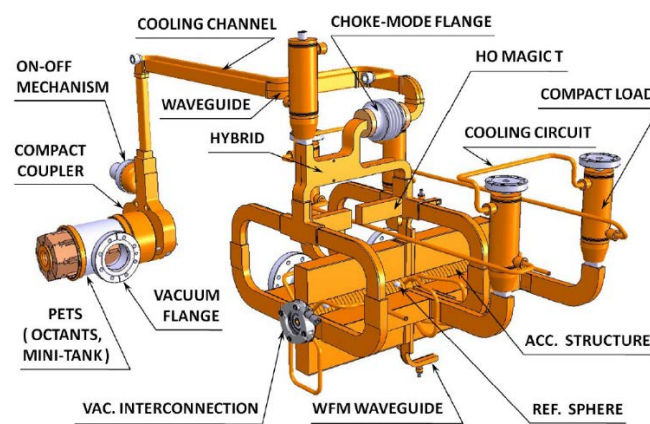


Figure 1.1. Schematic view of the CLIC module RF system

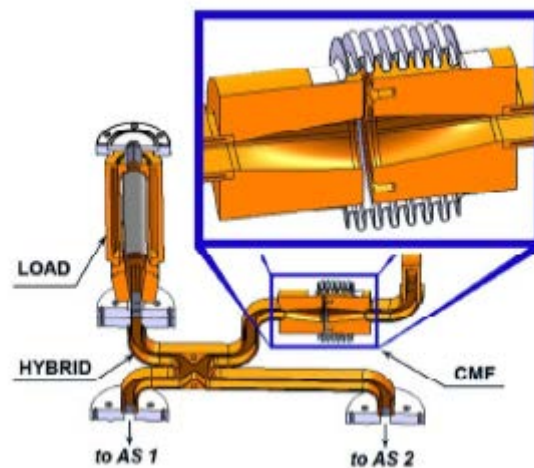


Figure 1.2. 3D model of the choke mode flange, hybrid and load

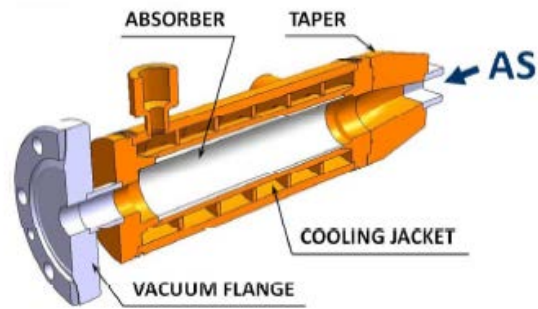


Figure 1.3. Schematic view of the CLIC 'dry' RF load

An RF load (see Fig. 1.3) is attached to one of the hybrid ports to avoid the reflection to the corresponding PETS, 5 of these loads are needed for each PET this makes the load the most common RF component, the requested load reduction factor is below -30db for a working frequency of approximately 12 GHz. The RF splitters are used to equally feed the accelerating structures.

Loads. Just few years before creating a compact load prototype would have been difficult, complexity and compactness of load models was often a problem for fabrication. Due to these reasons "old-generation" loads had dimensions that were way larger than the ones required. Nowadays thanks to the new 3-D printing technology, mainly electron-beam or laser-sintering based (for 3D printing methods descriptions see Appendix A) is easier to reach a better fabrication accuracy and is then possible to develop models and prototypes of compact loads. Nevertheless has to be considered that this new technology is still developing and, sometimes, prototypes are not satisfactory compared with expectations. Is thus a good habit to create a load with the simplest shape possible and that does not contain too complex features.

Old generation load. Old-generation load, developed for CLIC study high power X-band test stands.



Figure 1.4. Old-generation load

Several prototypes of this load have already been realized showing a good signal reduction, below -30 db, the main problem with this model is the length, approximately 0.9 m.

Compact Load. The compact load illustrated in Fig 1.2, is 10 cm long and is also called 'dry' RF load because the RF power is absorbed in a lossy ceramic (SiC) cylinder[8]. The model has not been fabricated and tested yet.

Goals. The goal of the work described in this thesis is the design of a load prototype that reaches a good reduction and a compact size with better performances than SiC compact load, design, radiofrequency simulations, and heating simulations are entirely implemented in ANSYS WORKBENCH[9] and ANSYS HFSS[10] interactive environments.

This page intentionally left blank

Chapter 2

Waveguides and Reflections

2.1 Theory of wave Propagation in Waveguides

Wave Propagation in waveguides, an Intuitive Introduction. A waveguide is a structure that guides waves, such as electromagnetic waves or sound waves. Consider now the ordinary power transmission line that is used for electricity transmission, this line radiates away some of its power, but since the frequencies are small losses are reasonable. If the frequency of electro-magnetic waves that are used for the transmission is increased losses would obviously higher. For frequencies from few kilocycles to some hundreds of megacycles, electromagnetic signals and power are usually transmitted via coaxial lines consisting of a wire inside a cylindrical ‘outer conductor’ or ‘shield’ (see Fig.2.1.1).

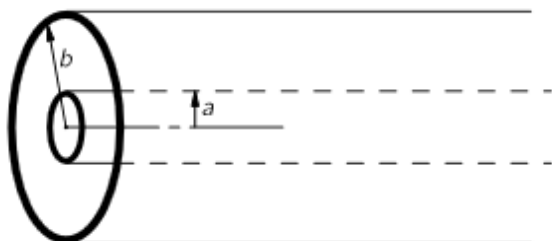


Figure2.1.1. Coaxial transmission line.

Imagine now that the central conductor is removed, will that be possible for an electromagnetic wave to propagate? Experience shows that if frequency is high enough a hollow tube will work as well as one with central conductor. This is not very impressive; as an example light propagation can be considered, is already known that it can travel along inside a hollow metal pipe, but is also known that low-frequency waves cannot. It is due to the cut-off frequency of the pipe. For frequencies below the cut-off, waves are not allowed for frequencies above they are. The coaxial transmission line without the central conductor represents a first simple model of waveguide[11],but ,in general, an hollow-pipe with any shape can be used as a waveguide.

Maxwell’s equation. Now on waveguides characterized by having axial uniformity will be studied. Their cross-sectional shape and electrical properties do not vary along the axis, which is chosen as the z axis. For waveguides Maxwell’s equations can be reformulated so as to describe three classes of waves, TEM, TE and TM waves. Since sources are not considered, the electric and magnetic fields are solutions of the homogeneous vector Helmholtz equations,

$$\nabla^2 \mathbf{E} + k_0^2 \mathbf{E} = 0 \quad \nabla^2 \mathbf{H} + k_0^2 \mathbf{H} = 0$$

Where \mathbf{E} , \mathbf{H} , and k_0 are the electric field, the magnetic intensity field and the free space wave number respectively. The type of solution sought is that corresponding to a wave that propagates along the z axis. The Helmholtz equation is separable so is possible to find a solution of the form $f(z)g(x, y)$, where the z dependence of the solution function is on the form $e^{-j\omega t}$, with ω angular frequency. This assumption will lead to have wave solutions of the form $\cos(\omega t \pm \beta z)$ and $\sin(\omega t \pm \beta z)$, with β propagation factor, which are appropriate for describing wave propagation along the z axis. A wave propagating in the positive z direction is represented by $e^{-j\beta z}$ and a wave propagating in the negative z negative direction is

represented by $e^{+j\beta z}$. With an assumed z dependence $e^{-j\beta z}$, the del operator becomes: $\nabla = \nabla_t + \nabla_z = \nabla_t - j\beta \mathbf{a}_z$, since $\nabla_z = \mathbf{a}_z \partial/\partial z$. Note that ∇_t is the transverse part and equals $\nabla_t = \mathbf{a}_x \partial/\partial x + \mathbf{a}_y \partial/\partial y$ in Cartesian coordinates. Considerable simplification of Maxwell's equations is obtained by decomposing all fields into transverse and axial components and separating out the z dependence. Thus let,

$$\mathbf{E}(x, y, z) = \mathbf{E}_t(x, y, z) + \mathbf{E}_z(x, y, z) = \mathbf{e}(x, y)e^{-j\beta z} + \mathbf{e}_z(x, y)e^{-j\beta z} \quad (2.1)$$

$$\mathbf{H}(x, y, z) = \mathbf{H}_t(x, y, z) + \mathbf{H}_z(x, y, z) = \mathbf{h}(x, y)e^{-j\beta z} + \mathbf{h}_z(x, y)e^{-j\beta z} \quad (2.2)$$

Where $\mathbf{E}_t, \mathbf{H}_t$ are the transverse (x and y) components and $\mathbf{E}_z, \mathbf{H}_z$ are the axial component. Note also that $\mathbf{e}(x, y), \mathbf{h}(x, y)$ are transverse vector functions of the transverse coordinates only, and $\mathbf{e}_z(x, y), \mathbf{h}_z(x, y)$ are axial vector functions of the transverse coordinates. Can be shown using Faraday's laws, and the properties of \mathbf{H}, \mathbf{B} and \mathbf{D} (electric displacement) fields, that following relations are valid:

$$\nabla_t \times \mathbf{e} = -j\omega\mu_0 \mathbf{h}_z \quad (2.3a)$$

$$\nabla_t \times \mathbf{e}_z - j\beta \mathbf{a}_z \times \mathbf{e} = -\mathbf{a}_z \times \nabla_t \mathbf{e}_z - j\beta \mathbf{a}_z \times \mathbf{e} = -j\omega\mu_0 \mathbf{h} \quad (2.3b)$$

$$\nabla_t \times \mathbf{h} = j\omega\varepsilon_0 \mathbf{e}_z \quad (2.3c)$$

$$\mathbf{a}_z \times \nabla_t \mathbf{h}_z + j\beta \mathbf{a}_z \times \mathbf{h} = -j\omega\mu_0 \mathbf{e} \quad (2.3d)$$

$$\nabla_t \cdot \mathbf{h} = j\beta \mathbf{h}_z \quad (2.3e)$$

$$\nabla_t \cdot \mathbf{e} = j\beta \mathbf{e}_z \quad (2.3f)$$

With ε_0 the vacuum permittivity and μ_0 the magnetic constant.

For a large variety of waveguides of practical interest it turns out that all the boundary conditions can be satisfied by fields that do not have all the component presents, specifically solutions with $\mathbf{E}_z=0$ or $\mathbf{H}_z=0$ are possible. Because of the widespread occurrence of such field solutions, the following classification of solutions is of particular interest[12].

Transverse electromagnetic (TEM) waves. For TEM waves, $\mathbf{E}_z=\mathbf{H}_z=0$. The electric field may be found from transverse gradient of a scalar function $\phi(x, y)$, which is a function of the transverse coordinates only and is a solution of the two-dimensional Laplace equation. In hollow waveguides, TEM waves are not possible, since Maxwell's Equations will give that the electric field must then have zero divergence and zero curl and be equal to zero at boundaries, resulting in a zero field.

Transverse magnetic (TM), or E modes. These solutions have $\mathbf{H}_z=0$, but $\mathbf{E}_z \neq 0$. The field components may be derived from \mathbf{E}_z .

Transverse electric (TE), or H modes. These solutions have $\mathbf{E}_z=0$, but $\mathbf{H}_z \neq 0$. All the field components may be derived from the axial component \mathbf{H}_z of magnetic field.[13]

TE modes. For transverse electric (TE) modes, h_z plays the role of a potential function from which the rest of the field may be obtained. The magnetic field \mathbf{H} is a solution of

$$\nabla^2 \mathbf{H} + k_0^2 \mathbf{H} = 0$$

Separating the above equation into transverse and axial parts and replacing ∇^2 by $\nabla_t^2 - \beta^2$ yield

$$\nabla_t^2 h_z(x, y) + k_c^2 h_z(x, y) = 0 \quad (2.4)$$

$$\nabla_t^2 \mathbf{h}(x, y) + k_c^2 \mathbf{h}(x, y) = 0 \quad (2.5)$$

Where $k_c^2 = k_0^2 - \beta^2$, with $k_0 = \omega\sqrt{\mu_0\epsilon_0}$ and $k_c = 2\pi f_c\sqrt{\mu_0\epsilon_0}$, and a z dependence $e^{-j\beta z}$ is assumed. When this equation is solved, subject to appropriate boundary conditions, the eigenvalue k_c^2 will be found to be a function of the waveguide configuration, with $\mathbf{e}_z=0$, equations 2.3 can be manipulated to obtain the solution for TE modes that are reported in compact form below:

$$\mathbf{h} = -\frac{j\beta}{k_c^2} \nabla_t h_z \quad (2.6a)$$

$$\mathbf{e} = -Z_h \mathbf{a}_z \times \mathbf{h} \quad (2.6b)$$

Where $\beta = \sqrt{k_0^2 - k_c^2}$ and $Z_h = \frac{k_0 Z_0}{\beta}$. Complete expressions for the fields are

$$\mathbf{H} = \pm \mathbf{h} e^{\mp j\beta z} + \mathbf{h}_z e^{\mp j\beta z} \quad (2.6c)$$

$$\mathbf{E} = \mathbf{E}_t = \mathbf{e}(x, y) e^{-j\beta z} \quad (2.6d)$$

2.2 Rectangular waveguide.

Maxwell's equations solution for rectangular waveguide. Explicit solutions for modes in a rectangular waveguide are now studied,

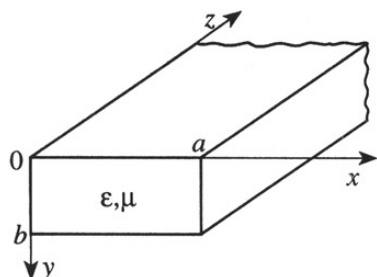


Figure 2.2.1. Rectangular waveguide.

The rectangular waveguide with a cross section as illustrated in Fig.2.2.1 is an example of a waveguiding device that will not support TEM wave (It is basically a hollow pipe).

As said before for TE, or H modes, $e_z=0$ and all the remaining field components can be determined from the axial magnetic field h_z . The axial field h_z is a solution of

$$\nabla_t^2 h_z(x, y) + k_c^2 h_z(x, y) = 0$$

Without proceeding in calculations results will directly be reported, these can be easily obtained if is considered that the normal component of the transverse magnetic field \mathbf{h} must vanish at the perfectly conducting waveguide wall, in the meaning that the x partial derivative of h_z has to be 0 at $x=0, a$ and the y partial derivative of h_z has to be 0 at $y=0, b$. For the nmth mode its cut-off wave number designated by $k_{c, nm}$ is obtained to be

$$k_{c, nm} = \sqrt{\frac{n\pi^2}{a} + \frac{m\pi^2}{b}} \quad (2.7)$$

In detail k_c is found to depend on m and n variables that can assume only positive integer values. For h_z holds the expression:

$$h_z = A_{nm} \cos \frac{n\pi x}{a} \cos \frac{m\pi y}{b} \quad (2.8)$$

Where A_{nm} is a constant that represents an arbitrary amplitude associated with the nmth mode. For the nmth mode cut-off frequency:

$$f_{c, nm} = \frac{c}{2\pi} k_{c, nm} = \frac{c}{2\pi} \sqrt{\left(\frac{n\pi}{a}\right)^2 + \left(\frac{m\pi}{b}\right)^2} \quad (2.9)$$

At this point the remainder of the field components for TE_{nm} , or H_{nm} , mode are readily found from 2.8, by using 2.3 and 2.6.

The results for the complete nmth solution are

$$H_z = A_{nm} \cos \frac{n\pi x}{a} \cos \frac{m\pi y}{b} e^{\mp j\beta_{nm} z} \quad (2.10a)$$

$$H_x = \pm j \frac{\beta_{nm}}{k_{c,nm}^2} A_{nm} \frac{n\pi}{a} \sin \frac{n\pi x}{a} \cos \frac{m\pi y}{b} e^{\mp j\beta_{nm}z} \quad (2.10b)$$

$$H_y = \pm j \frac{\beta_{nm}}{k_{c,nm}^2} A_{nm} \frac{m\pi}{b} \cos \frac{n\pi x}{a} \sin \frac{m\pi y}{b} e^{\mp j\beta_{nm}z} \quad (2.10c)$$

$$E_x = Z_{h,nm} A_{nm} j \frac{\beta_{nm}}{k_{c,nm}^2} \frac{m\pi}{b} \cos \frac{n\pi x}{a} \sin \frac{m\pi y}{b} e^{\mp j\beta_{nm}z} \quad (2.10d)$$

$$E_y = -Z_{h,nm} A_{nm} j \frac{\beta_{nm}}{k_{c,nm}^2} \frac{n\pi}{a} \sin \frac{n\pi x}{a} \cos \frac{m\pi y}{b} e^{\mp j\beta_{nm}z} \quad (2.10e)$$

Where the impedance for the nmth H mode is given by

$$Z_{h,nm} = \frac{k_0}{\beta_{nm}} Z_0 \quad (2.11)$$

When the mode does not propagate, $Z_{h,nm}$ is imaginary, indicating that there is no net energy flow associated with the evanescent mode. Moreover generally speaking, a field with $E_z = 0$ can be described in a complete manner by a linear superposition of all the H_{nm} modes.

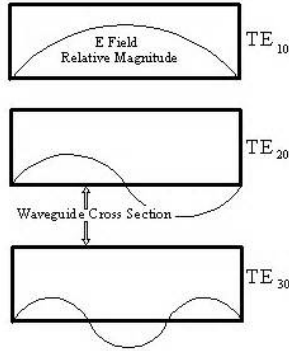


Figure 2.2.2. Electric field distribution for the first three TE_{n0} modes in a rectangular waveguide.

Power. For a propagating H_{nm} mode the power, or rate energy flow, in the positive z direction is given by

$$P_{nm} = \frac{1}{2} \text{Re} \iint_{0,0}^{a,b} \mathbf{E} \times \mathbf{H}^* \cdot \mathbf{a}_z dx dy \quad (2.12)$$

And for a rectangular waveguide substituting in 2.12 the expressions 2.10b, 2.10c,

$$P_{nm} = \frac{|A_{nm}|^2 ab}{2\epsilon_{0n}\epsilon_{0m}} \left(\frac{\beta_{nm}}{k_{c,nm}} \right)^2 Z_{h,nm} \quad (2.13)$$

Where ϵ_{0m} is the Neumann factor and equal to 1 for $m=0$ and equal to 2 for $m > 0$. [14]

Attenuation, H₁₀ mode. If the waveguide walls have a finite conductivity, there will be a continuous loss of power to the walls as the modes propagate along the guide. Consequently, the phase constant $j\beta$ is perturbed and becomes $\gamma = \alpha + j\beta$, where α is an attenuation constant that gives the rate at which the mode amplitude must decay as the mode progresses along the waveguide. For practical waveguides the losses caused by finite conductivity are so small that the attenuation constant may be calculated using the perturbation method. Here this method is used for the H₁₀ mode only. For the H₁₀ mode, the fields are given by (apart from the factor $e^{-j\beta_{10}z}$),

$$h_z = A_{10} \cos \frac{\pi x}{a} \quad (2.14)$$

$$h_x = j \frac{\beta_{10}}{k_{c,10}^2} A_{10} \frac{\pi}{a} \sin \frac{\pi x}{a} \quad (2.15)$$

$$e_y = -Z_{h,10} A_{10} \frac{j\beta_{10}}{k_{c,10}^2} \frac{\pi}{a} \sin \frac{\pi x}{a} \quad (2.16)$$

From 2.13 the rate of energy flow along the guide is

$$P_{10} = \frac{|A_{10}|^2 ab}{4} \left(\frac{\beta_{10}}{k_{c,10}} \right)^2 Z_{h,10} \quad (2.17)$$

The current on the lossy walls are assumed to be the same as the loss-free currents, and hence are given by

$$\mathbf{J}_s = \mathbf{n} \times \mathbf{H} \quad (2.18)$$

Where \mathbf{n} is a unit inward directed normal at the guide wall. Thus, on the walls at $x=0, a$ the surface currents are

$$\mathbf{J}_s = \begin{cases} \mathbf{a}_x \times \mathbf{H} = -\mathbf{a}_y A_{10} & ; x = 0 \\ -\mathbf{a}_x \times \mathbf{H} = -\mathbf{a}_y A_{10} & ; x = a \end{cases} \quad (2.19)$$

Whereas on the upper and lower walls the currents are

$$\mathbf{J}_s = \begin{cases} \mathbf{a}_y \times \mathbf{H} = -\mathbf{a}_z \frac{j\beta_{10}}{k_{c,10}^2} \frac{\pi}{a} \sin \frac{\pi x}{a} A_{10} + \mathbf{a}_x A_{10} \cos \frac{\pi x}{a} & ; y = 0 \\ -\mathbf{a}_y \times \mathbf{H} = \mathbf{a}_z \frac{j\beta_{10}}{k_{c,10}^2} \frac{\pi}{a} \sin \frac{\pi x}{a} A_{10} - \mathbf{a}_x A_{10} \cos \frac{\pi x}{a} & ; y = b \end{cases} \quad (2.20)$$

With a finite conductivity σ , the waveguide walls may be characterized as exhibiting a surface impedance given by

$$Z_m = \frac{1+j}{\sigma \delta_s} = (1+j)R_m \quad (2.21)$$

Where δ_s is the skin depth. The power loss in the resistive part R_m of Z_m per unit length of guide is:

$$P_l = \frac{R_m}{2} \oint_{\text{walls}} \text{guide } \mathbf{J}_s \cdot \mathbf{J}_s^* dl \quad (2.22)$$

With $k_{c,10} = \pi/a$, the above gives

$$P_l = R_m |A_{10}|^2 \left[b + \frac{a}{2} \left(\frac{\beta_{10}}{k_{c,10}} \right)^2 + \frac{a}{2} \right] \quad (2.23)$$

If P_0 is the power at $z=0$, then $P_{10} = P_0 e^{-2\alpha z}$ is the power in the guide at any z , it's interesting to notice that P_{10} undergoes an exponential decay. The rate of decrease of power propagated is

$$-\frac{dP_{10}}{dz} = 2\alpha P_{10} = P_l \quad (2.24)$$

And equals the power loss, as indicated in the above equation. The attenuation constant α for the H_{10} mode is thus seen to be

$$\alpha = \frac{P_l}{2P_{10}} = \frac{R_m}{ab\beta_{10}k_0Z_0} (2bk_{c,10}^2 + ak_0^2) \quad (2.25)$$

and its usually expressed in Np/m (Neper/meter) or in db/m (decibel/m)[15].

2.3 Scattering parameters

Two-port junction. Consider now a 2-port junction (a 2-port waveguide is an example) this device can be studied through a circuit framework approximation (see Fig.2.3.1)

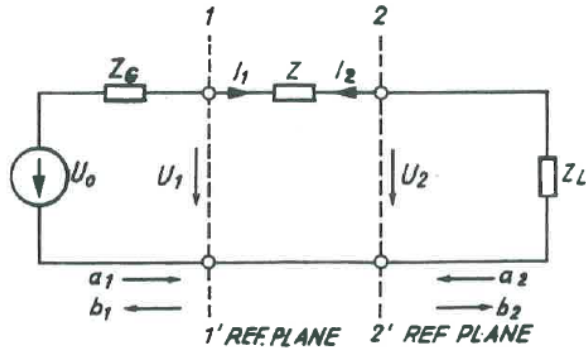


Figure2.3.1. 2-port network.

If $Z=0$ and $Z_G=Z_L$ (with Z_G and Z_L real) matched load conditions are fixed and $U_1=U_2=U_0/2$. The lines connecting the different elements (Z_G, Z_L, Z) in Fig.2.3.1 are supposed to have no electrical length. The goal is to relate voltages U_0, U_1, U_2 with a and b .

All waves going towards the n-port are a (a_1, a_2, \dots, a_n). All waves travelling away from the n-port are b (b_1, b_2, \dots, b_n). The definition for the direction of the currents (generalization for n-port) says that positive currents flow into the network as in Fig.2.3.3. The wave a_1 is related to the maximum available power (matched load).

In order to give definitions that are consistent with the conservation energy, the voltage is normalized to $\sqrt{Z_0}$. Z_0 is in general an arbitrary reference impedance, but is usually the characteristic impedance of a line (e.g. 50 Ω) and very often $Z_G=Z_L=Z$.

$$a_1 = \frac{U_0}{2\sqrt{Z_0}} = \frac{\text{incident voltage wave (port 1)}}{\sqrt{Z_0}} = \frac{U_1^i}{\sqrt{Z_0}} \quad (2.26)$$

$$b_1 = \frac{U_1^r}{\sqrt{Z_0}} = \frac{\text{reflected voltage wave (port 1)}}{\sqrt{Z_0}} \quad (2.27)$$

Note that a, b have the dimensions of $\sqrt{\text{power}}$

The power travelling towards port 1 is simply the available power from the source, i.e.

$$P_1^i = \frac{1}{2} |a_1|^2 \quad (2.28)$$

$$P_1^r = \frac{1}{2} |b_1|^2 \quad (2.29)$$

In the case of mismatched load Z_L there will be some power reflected towards the 2-port (from Z_L).

$$P_2^i = \frac{1}{2} |a_2|^2 \quad (2.30)$$

$$P_2^r = \frac{1}{2} |b_2|^2 \quad (2.31)$$

In general as described in previous section in this condition holds a system of the form:

$$b_1 = S_{11}a_1 + S_{12}a_2 \quad (2.32)$$

$$b_2 = S_{21}a_1 + S_{22}a_2. \quad (2.33)$$

The physical meaning of S_{11} is the input reflection coefficient with the output of the network terminated by a matched load ($a_2=0$). S_{21} is the forward transmission (from port 1 to port 2), S_{12} the reverse transmission and S_{22} the output reflection coefficient.

So when measuring the S-parameters of an n-port, all n ports must be terminated by a matched load, including the port connected to the generator. So for example for S_{11} we can write:

$$S_{11} = \left(\frac{b_1}{a_1} \right)_{a_2=0} \quad (2.34)$$

or using the correlation with the power we found before:

$$|S_{11}| = \sqrt{\frac{P_1^r}{P_1^i}} \quad (2.35)$$

In the same way we can define:

$$S_{12} = \left(\frac{b_1}{a_2} \right)_{a_1=0} ; S_{21} = \left(\frac{b_2}{a_1} \right)_{a_2=0} ; S_{22} = \left(\frac{b_2}{a_2} \right)_{a_1=0} \quad (2.36)$$

In case of a symmetric homogeneous 2-port waveguide as discussed in previous section the scattering matrix is symmetric:

$$S_{11}=S_{22}; S_{12}=S_{21} \quad [16] \quad (2.37)$$

Example

For a TE₁₀ mode propagating in a rectangular 2-port waveguide with input power P_0 using 2.24 , S_{21} expression from equation 2.37 takes the simple form of

$$|S_{21}| = \sqrt{\frac{P_{10}}{P_0}} = e^{-\alpha z} \quad (2.38)$$

Waveguides in series. Following the previous example, if instead of a unique waveguide, k waveguides in series are considered and the total reflection equals 0, the total S_{12} parameter can be written as

$$|S_{12tot}| = \prod_1^k |S_{12n}| \quad (2.39)$$

If the Scattering parameter is expressed in Np and

$$S_{12tot} = \sum_1^k S_{12n} \quad (2.40)$$

If the scattering parameter is expressed in dB, where S_{12n} is the scattering parameter of the n th waveguide.

Scattering parameters reminder. Was shown before a simple way to express the scattering parameters in function of the power (see 2.38), nevertheless through this formula only the absolute value of the scattering parameter is obtained and information about the phase is lost. In fact is worth to underline that the scattering parameter is a complex number.

The phase of the scattering parameter is not discussed here in detail, but this argument will be of crucial importance in Chapter 4.

This page intentionally left blank

Chapter3

RF Load Model

3.1. Application of the concepts to rectangular waveguides

Introduction. In previous chapter a complete set of equations for propagating waves in rectangular waveguides has been given with a main focus on TE_{10} mode propagation. In the following chapter only these waveguides and modes are studied, the TE_{10} is the only mode excited in the waveguides, with the working frequency of 12 GHz that is the working frequency of CLIC accelerator.[17] A main focus is given to two-ports and one-port devices with an axial symmetry along z .

In this chapter is first conducted a brief study of 2-port rectangular waveguides the relative S_{12} parameter. This parameter is of particular interest because, for a two-port waveguide, S_{11} and S_{22} , corresponding to the reflected wave at the first port and at the second respectively, are so low (this consideration is valid for rectangular straight waveguide but is not a general statement) that can be in first approximation considered 0. Moreover given the symmetry of the waveguiding devices, thus the one of the scattering matrix, calculating S_{12} , S_{21} is automatically known.

Simulations in HFSS. As specified in the beginning ANSYS HFSS is used for RF simulations. Some of the pictures reported in this chapter and chapter 4 are taken from this interactive environment and require some explanations. A waveguide is practically void inside and is possible in HFSS to implement simulations using the so called vacuum part, corresponding to the internal part of the waveguide. On the surface of the vacuum part (vacuum model) are applied boundary conditions that represent the conductivity of the material. The HFSS pictures that are reported have therefore always to be considered as the internal part of the waveguide, the waveguide itself is not shown.

Narrow waveguide. A straight narrow rectangular waveguide is first analysed, with symmetry along z -axis and following dimensions, $a=13\text{mm}$, $b=2\text{mm}$, this waveguide is called "narrow" waveguide because has smaller dimensions than the ones that are introduced later. Can be seen from Eq. 2.25 that the attenuation constant α depends only on a and b and then, for a given length, Eq. 2.38 can be used to calculate the scattering parameter for the TE_{10} mode. Scattering parameter S_{12} evolution in function of length is analytically found this way, as a comparison are below reported also S_{12} values obtained through HFSS simulations for the same waveguide.

Length (m)	S_{12} (Np) Analytical	S_{12} (Np) HFSS
0.2	0.71177	0.71369
0.4	0.50661	0.50775
0.6	0.36059	0.36347
0.8	0.25666	0.25545
1	0.18268	0.18515
1.2	0.13002	0.13113
1.4	0.09255	0.09429
1.6	0.06587	0.06236
1.8	0.04688	0.04751
2	0.03337	0.03328

Table 3A. S_{12} parameter narrow waveguide.

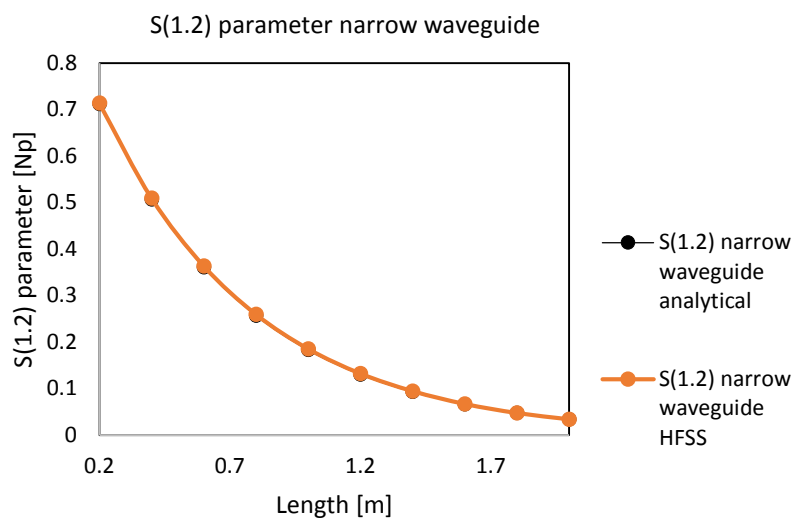


Figure 3.1.1 S_{12} parameter plot narrow waveguide

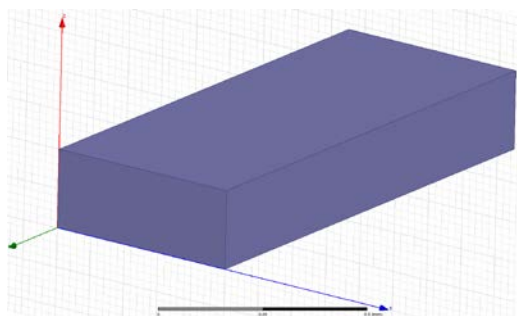


Figure 3.1.2. Narrow rectangular waveguide model in HFSS.

Can be seen from data that results obtained through simulations are in good agreement with the analytical model.

WR90 waveguide. Using the same procedure followed for the narrow waveguide and changing dimensions that are the ones of a standard waveguide also called WR90[18], new analytical and simulations values of S_{12} are calculated and reported below. WR90 dimensions are, $a=22.86\text{mm}$, $b=10.16\text{mm}$.

Length (m)		S_{12} (Np) analytical	S_{12} (Np) HFSS
0.2		0.97706	0.97683
0.4		0.95466	0.95421
0.6		0.93276	0.93210
0.8		0.91137	0.91053
1		0.89047	0.88942
1.2		0.87005	0.86880
1.4		0.85010	0.84873
1.6		0.83060	0.82902
1.8		0.81155	0.80986
2		0.79294	0.79111

Table 3B. S_{12} parameter WR90 waveguide.

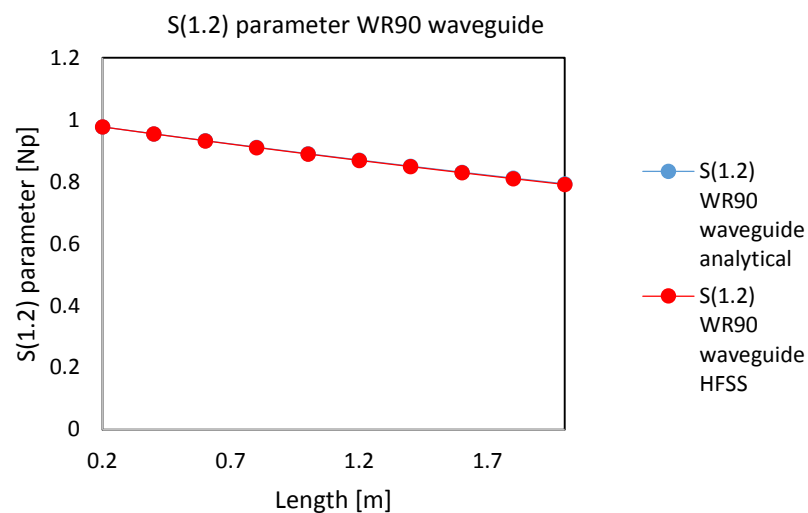


Figure3.1.3 S_{12} parameter plot WR90 waveguide

Once again can be noticed a good agreement between the analytical model and HFSS.

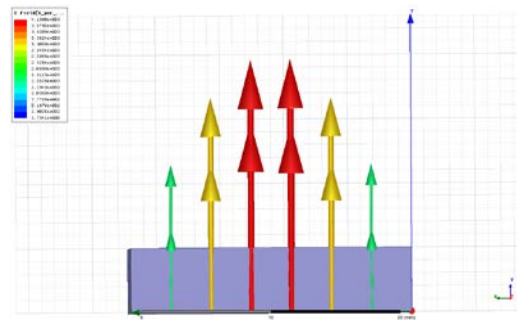


Figure3.1.4. TE_{10} mode in WR90 waveguide. See also Fig.2.1.2.

Tapered Waveguide. Is now introduced a more complex model of waveguide, generally called tapered waveguide, which cross section dimensions linearly grow from fixed values a_0 and b_0 to a_1 , b_1 .

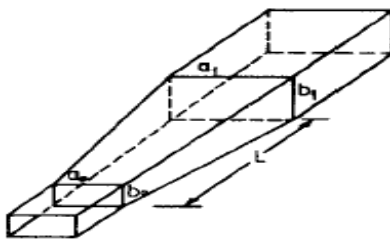


Figure3.1.5. Tapered waveguide.

Chosen values for a_0 and b_0 are the ones relative to the narrow waveguide analysed before and a_1 , b_1 relative to a WR90 waveguide also studied previously.

The problem in this case is that there is not an analytical model that describes the evolution of the scattering parameter through the waveguide. The solution to the problem is reached using an approximation-method here described in detail.

Consider the tapered waveguide as a set of many little straight rectangular waveguides with fixed values of a and b disposed in series. Obviously the bigger is the number of ‘bricks’ used the better is the approximation of the volume. For an infinite number of bricks the tapered waveguide itself would be obtained. If the tapered waveguide is divided in N bricks formula 2.41 might be used (that is valid for waveguides in series with 0 reflection) to calculate the total scattering parameter as a finite product of parameters.

In practice a_0 and b_0 are assigned as the width and depth of the smallest cross section respectively, and a_1 and b_1 for the biggest one. Can be noticed that the vertexes of the two faces are connected by lines and therefore grow linearly, this means that the cross section of the waveguide also grows linearly.

Expression for the values of the n th a and b relative to the n th brick become:

$$a_n = a_0 + \frac{(a_1 - a_0)}{N} n \quad (3.1)$$

$$b_n = b_0 + \frac{(b_1 - b_0)}{N} n \quad (3.2)$$

Where N represents the total number of bricks chosen for the approximation, can be seen that for n=0 values obtained are the ones relative to the narrow waveguide, a_0 and b_0 , and that for n=N, values are a_1 b_1 that are the ones of the WR90 waveguide.

For next numerical calculations N is set equal to 300 and a script is created in Octave[19] in order to calculate S_{12} . Are reported below plot and values obtained numerically and through simulations for different waveguide lengths,

Length (m)	S_{12} (Np) analytical	S_{12} (Np) HFSS
0.2	0.92844	0.92572
0.4	0.862	0.86385
0.6	0.80031	0.80753
0.8	0.74304	0.75137
1	0.68987	0.70064
1.2	0.6405	0.65355
1.4	0.59467	0.60938
1.6	0.55211	0.56815
1.8	0.5126	0.5298
2	0.47616	0.49449

Table 3C. S_{12} parameter tapered waveguide.

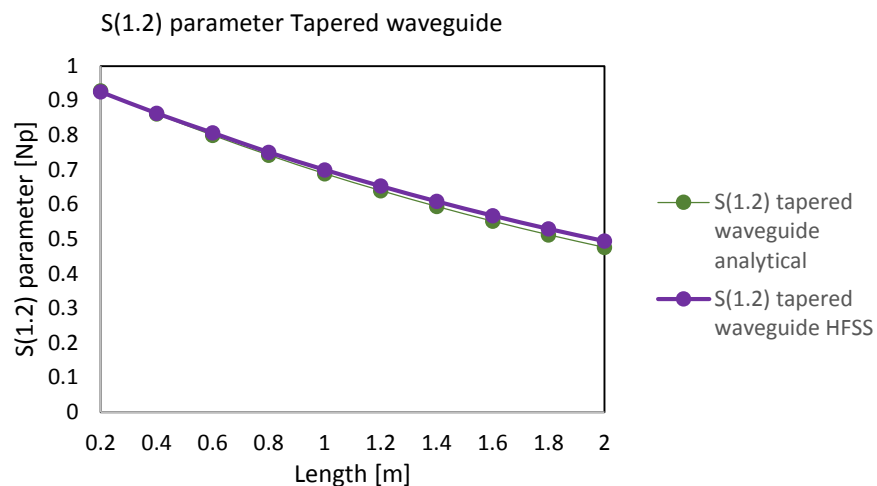


Figure 3.1.6. S_{12} parameter plot tapered waveguide

Final Considerations. As a final comparison the plot of the three curves (analytical data) obtained for S_{12} is reported below,

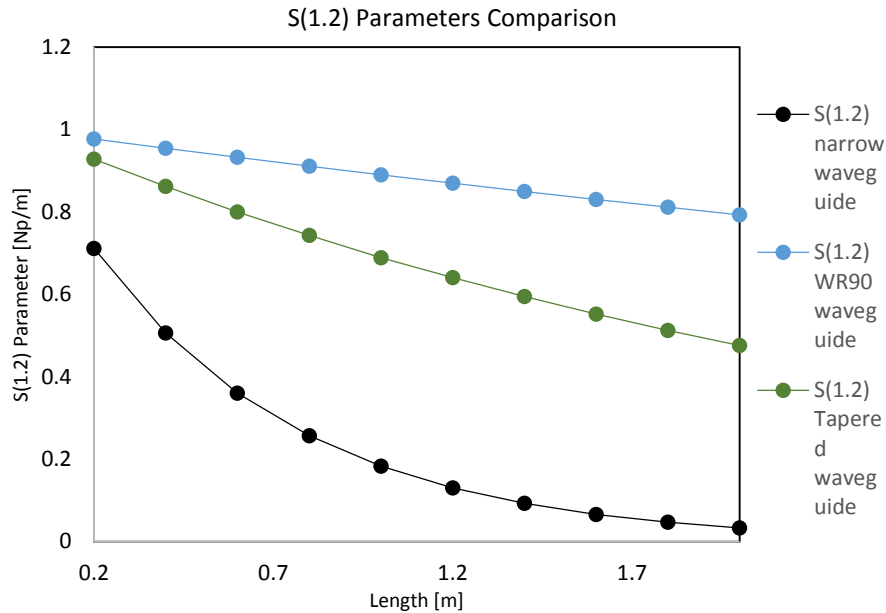


Figure 3.1.7. S_{12} parameter comparison plot for three waveguides

Can be seen from the plot that the narrow waveguide gives the highest attenuation, the WR90 the lowest and that the tapered waveguide has reduction values that are in between the two..

3.2 RF load model

Waveguides and associated loads. A load is basically a damper that in our specific case is used as a microwaves absorber. Given a 2-port waveguide, as those studied in previous section, one of the two ports may be closed to obtain a load. In this scenario electromagnetic waves (microwaves in this case) entering the load would be reflected back at the end of the load going through a round-trip, producing a dissipation that is double the one obtained with the propagation through the waveguide. The more the dissipation (quantified by the reflection coefficient) the more efficient the load would be considered. For a load only a scattering parameter is studied labelled by (1.1) corresponding to the only element of the scattering matrix.[20]

For a regular 2-port waveguide were given 4 corresponding scattering parameters and for a load only one. Analysing the physical situation can be seen that the S_{11} parameter of a load, in relation to the corresponding waveguide, can be calculated using formulas 2.40, 2.41. Resulting correlations are:

$$S(1.1)_{Np/m} = S(1.2)_{Np/m} S(2.1)_{Np/m} \quad (3.3)$$

$$S(1.1)_{dB} = S(1.2)_{dB} + S(2.1)_{dB} \quad (3.4)$$

Again given the symmetry of the scattering matrix:

$$S(1.1)_{Np/m} = S(1.2)_{Np/m}^2 = S(2.1)_{Np/m}^2 \quad (3.5)$$

$$S(1.1)_{dB} = S(1.2)_{dB} + S(1.2)_{dB} = S(2.1)_{dB} + S(2.1)_{dB} = 2 S(1.2)_{dB} \quad (3.6)$$

Intuitively a travelling wave in a load, is equivalent to a wave that first crosses the relative waveguide with an $S(1.2)$ parameter, and then if the second port is closed at the moment the travelling wave joins the other edge of the waveguide, travels back with the related $S(2.1)$ parameter.

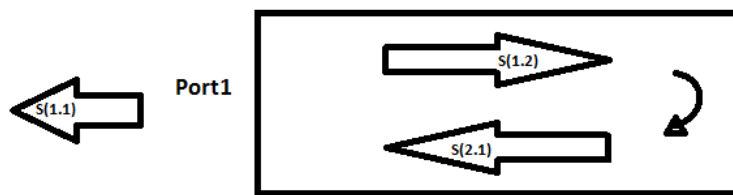


Figure 3.2.1. Scattering parameters for a load and related waveguide

S_{12} parameter was found for three waveguides in previous chapter. These waveguides properties as loads will be discussed below.

Thanks to Eq. 3.6 is known that the scattering parameter of these loads (in dB) is double of the value of the S_{12} parameters calculated before. Thus, is also known that the highest attenuation (the smallest value of S_{11}) would be given by a waveguide with as small as possible values of a and b . The problem using a "narrow" waveguide is that its tolerance to power might be very low, in fact power undergoes an exponential decay in this case, in particular this means that the initial part of the waveguide would be surely overheated. A "big" waveguide on the other hand would tolerate more power but the attenuation obtained for a given length could not be satisfactory as seen in previous section for WR90 waveguide. The tapered waveguide described in previous section can be of use in this case. Power density for a tapered waveguide is reasonably well distributed given a sufficient length, and in the reflection coefficient calculation was seen that is reached a better reduction than the one of the WR90 waveguide.

Consider now connecting a tapered waveguide to a narrow waveguide to create a load.

The biggest cross section of the tapered waveguide is chosen as the input port. In this way an overheating at the very beginning of the load can be avoided and then, waves would be easily dissipated after reaching the small waveguide. This briefly described configuration represents the first model of load here analysed. In order to reach a reduction of -30db is decided to use a combination of the tapered and straight waveguides for a total S_{12} parameter of -15 db and then made the same considerations had before, obtain a load with S_{11} of -30db. A length 1.5m is chosen for the tapered waveguide with dimensions $a_1=22.86$ $b_1=5.08$, and 0.69m for the straight waveguide with $a_0=13$, $b_0=2$, that according to analytical studies lead to the right reduction factor. We can create the model discussed above in HFSS and see if the results we expect are in agreement with simulations:

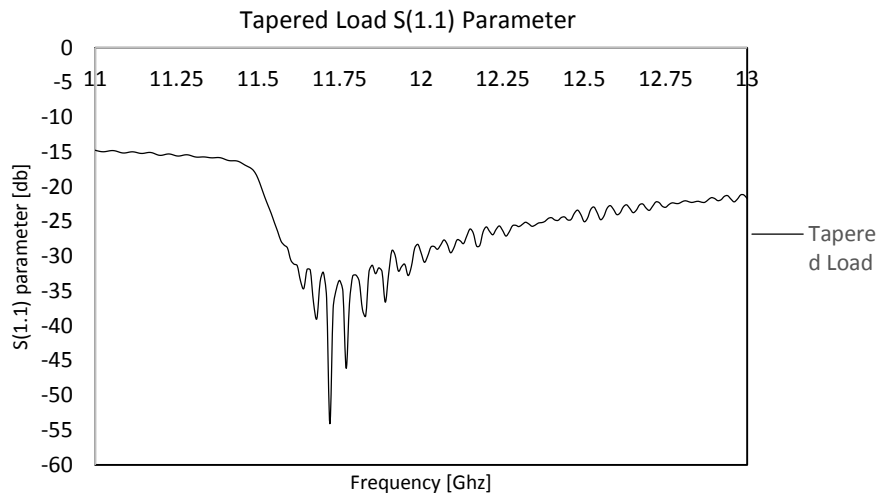


Figure3.2.2. S_{11} parameter plot tapered load

Indeed can be seen from the Fig.3.2.2 that HFSS model provides the required reflection of -30dB at 12 GHz,.

Roughness. In the remainder of the document we will not make statistics error calculations. Models implemented in HFSS behave as perfect conductors with perfect finite conductivity but in practice, surface is never smooth and contains imperfections that create higher RF power losses into heat than the one of a perfect conductor[21]. This irregularity of surface is often called roughness and can be quantified and the effect can be simulated in HFSS.

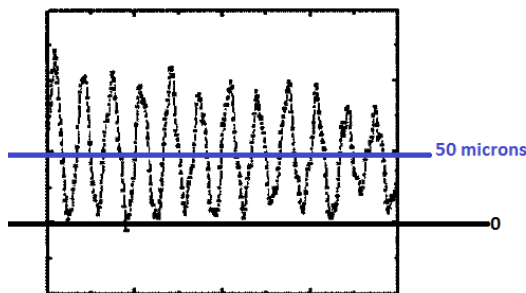


Figure3.2.3. Average Roughness, the value of 50 microns is typically obtained in additively manufactured parts from Ti6Al4V

Comparing the two surfaces shown in Fig.3.2.3 we can consider the excursions from the ideal waveguide surface. The average value of these excursions will be assigned to be the average value of roughness. The value implemented in HFSS is the one given by several studies on Ti6Al4V alloy, estimated to be 50 μm [22].

Due to this factor, losses for “rough” surfaces are always higher than the ones for smooth surfaces. Therefore simulations without roughness give an upper limit of the value that S_{11} can reach and simulations with roughness a lower one. Can be expected that the measured value of S_{11} will be in between these two limits depending on the roughness parameter.

Adding Roughness to the model. Roughness factor is added in HFSS and simulations are ran,

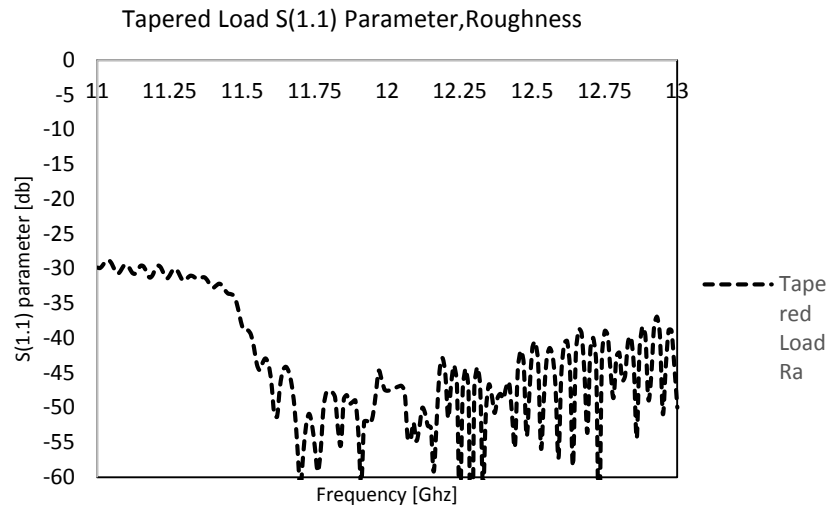


Figure 3.2.4. S_{11} parameter plot tapered load, Roughness

In this case attenuation at 12 GHz is increased (see Fig.3.2.4). In the legend of the plot the roughness factor is labelled by Ra.

Final Considerations

This model of load shows a good reduction coefficient, the main problem is given by the dimensions (2.19 meters length). As said in the beginning these loads will be placed in series in the LINAC and considering the length of the single load the length needed for the linac would be too big.

This page intentionally left blank

Chapter 4

Spiral Load

4.1 Geometry Description

Main ideas. The goal of this study is to create a load that provides low reflection but that occupies little space, one of the options is to change the shape and the concept of the load model described in previous chapter. The risk in changing the shape of the tapered load is to generate a larger reflection.

The solution to the problem comes letting evolve the tapered load along a spiral polyline, in the sense that the load can be compacted on a spiral shape. As said before this could change the scattering properties of the load itself, moreover there is not an analytical model for a spiral load and has also to be considered that the compactness of the load may generate an overheating and a consequential deformation.

Study is be developed following at first RF simulations for the spiral load, these results are then compared with the ones obtained for the tapered load. After RF simulations also thermal simulations are implemented in order to check that the new prototype does not overheat or deform.

In next sections is not presented an analytical model study anymore, because as said before there is not a valid one for a load with a spiral shape. Therefore only simulations results are reported and is assumed that they describe well the model, in the way the previous simulations did. The spiral load design and analysis is be described from the very beginning, all the details are listed and all the steps taken during the realization are described in following sections.

Specifics of the spiral load. Building the spiral load some practical details have to be considered. A vacuum pump is needed to maintain vacuum inside, the standard vacuum pump flange has usually a cylindrical shape with a radius of 10mm. As said before the load evolves along a spiral polyline, thus at first a polyline that approximately keeps the length of the tapered load has to be created. Another important observation is that the thickness for the walls of the load has to be 2mm.

Is worth to remember that the straight load is composed by a tapered waveguide joint with a straight waveguide, so the spiral polyline has to be a combination of two spirals, one with a linear growth and one with a non-linear growth. Finally the polyline has to be built in the simplest possible way, because it has to be reproducible in other virtual environments such as: CATIA[23], CST[24], etc...For this reason the spiral polyline is built in series of semicircles.

The spiral polyline. As already said a vacuum pump connection is needed, for homogeneity and symmetry the pump is fixed in the centre of the load. This fixes the first radius of the spiral polyline that will thus also be of 10mm. For the straight part of the spiral radii are described by the following series,

$$R_n = 10 + 2n \quad (4.1)$$

Where dimensions of radii are in mm. The factor 2 is given by the the thickness of walls.

For the straight part a length of 0.69m is required,

$$L_{tot} = 10k + \sum_{n=1}^k 2n = 10k + 2 \left(\frac{k(k+1)}{2} \right) \quad (4.2)$$

Equating the last expression to 690mm (0.69m), k can be calculated, this number represents the total number of semicircles needed. k is found to be 11.

Label		Radii Length (mm)
0		10
1		12
2		14
3		16
4		18
5		20
6		22
7		24
8		26
9		28
10		30

Table 4A. List of radii of semicircles for linear-growing spiral

For the tapered waveguide the growth cannot be linear. The chosen length for the tapered waveguide is 1.5 meters that corresponds to 1500mm and the difference between the two last radii has to be 3.54mm (remember that for the tapered waveguide $a_1=5.08\text{mm}$, that for the polyline will be the difference between last two diameters, taking into account the thickness we see that $3.54=(5.08+2)/2$).

Hypothesizing that the growth of radii for this part of the polyline is quadratic radii follow the series,

$$R_n = 30 + an^2 \quad (4.3)$$

Where 30 is the value of the last radius of the linear-growing spiral and a is a constant to be determined. Given this formula for radii the total correspondent length has the analytical expression:

$$L_{tot} = 30k + \sum_{n=1}^k an^2 = 30k + a \left(\frac{(k+1)(k+2)}{2} \right) \quad (4.4)$$

Imposing this expression equal to 1500 (mm) and also using the boundary-condition ($R_k - R_{k-1} = 3.54$). Is then obtained $a=0.71$, and $k=11$.

Label		Radii Length (mm)
0		32.071
1		34.284
2		36.639
3		39.639
4		39.136
5		41.775
6		44.556
7		47.479
8		50.544
9		53.751
10		57.1
11		60.591

Table 4B. List of radii for non- linear-growing spiral

Is then possible to proceed to the construction of the spiral polyline, and sweep a rectangle of 2mm thickness around the polyline in order to obtain the walls of the waveguide load,

Figure 4.1.1. Spiral polyline, on the left.

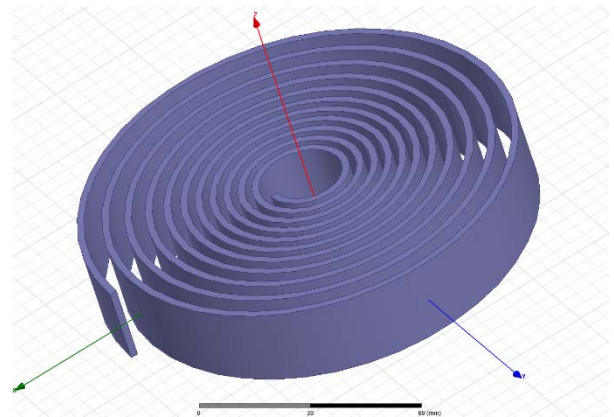
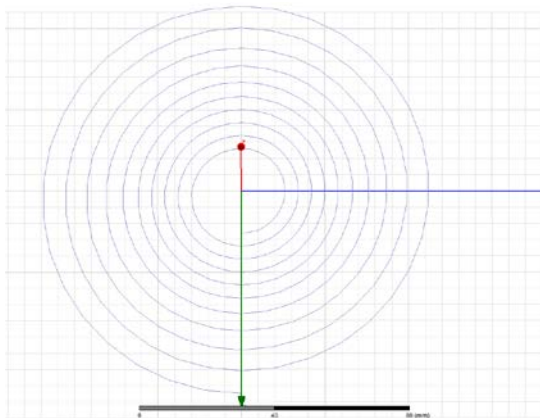


Figure 4.1.2. Spiral load walls.

If a box with adequate dimensions is created and then the volume created in last step is subtracted the spiral internal part (vacuum part) shown in Fig 4.0.2 is finally obtained.

Spiral load..

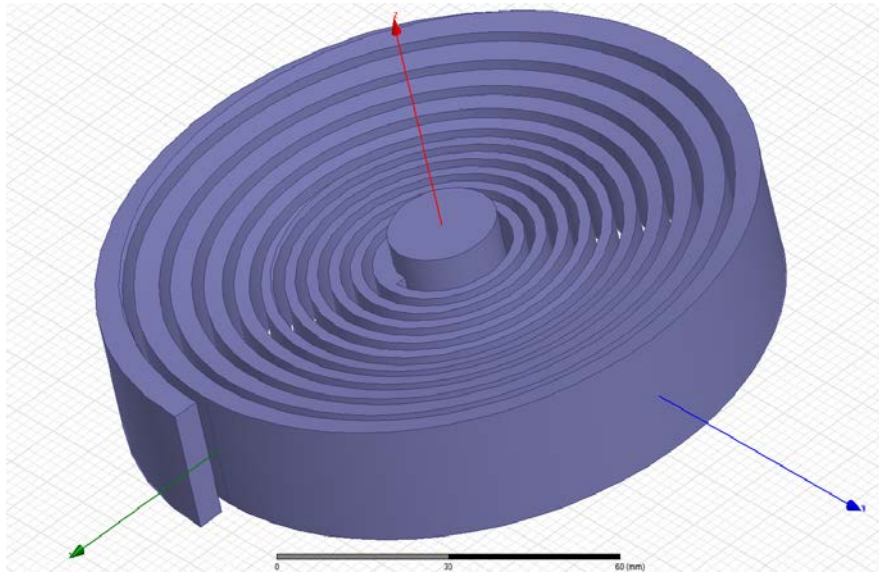


Figure 4.1.3. Spiral after subtraction, vacuum model.

Simulations for this model are ran to check compatibility with the requested reduction factor, and compatibility with the reduction factor of the tapered straight load.

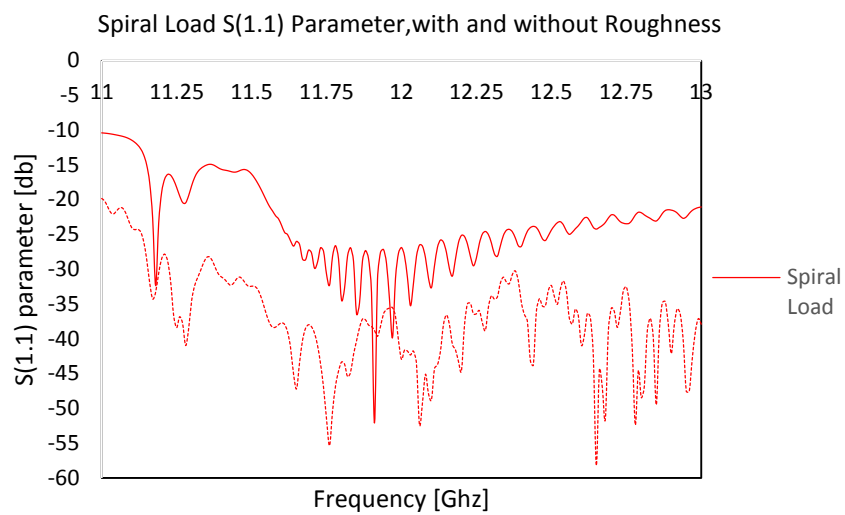


Figure 4.1.4. S₁₁ parameter plot for spiral load , with and without Roughness

Can be seen in Fig. 4.1.4 that in this case the reduction factor for 12 GHz is higher than -30db without Roughness factor, this is due to the curvature of the spiral that generates higher reflection from the very beginning of the waveguide, however adding the roughness factor a satisfactory result is reached. The comparison between the tapered load and the spiral load is shown in Fig. 4.1.5 and 4.1.6:

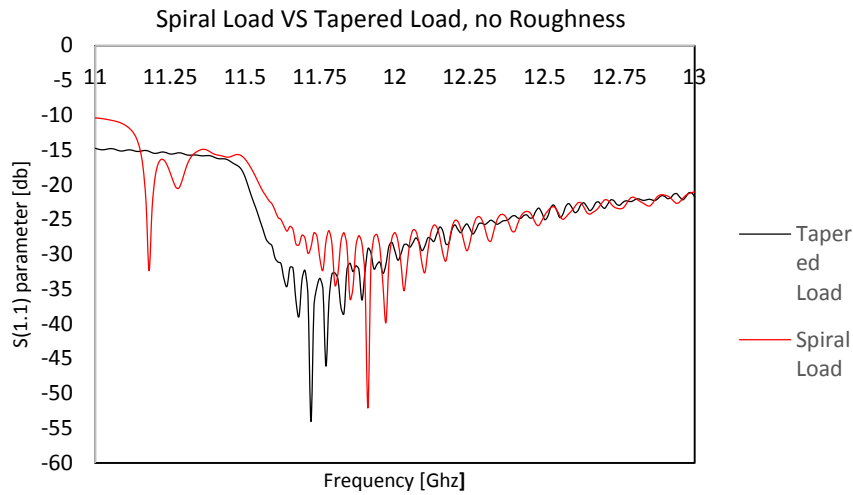


Figure 4.1.5. S_{11} parameter comparison between spiral and tapered load, HFSS, no Roughness

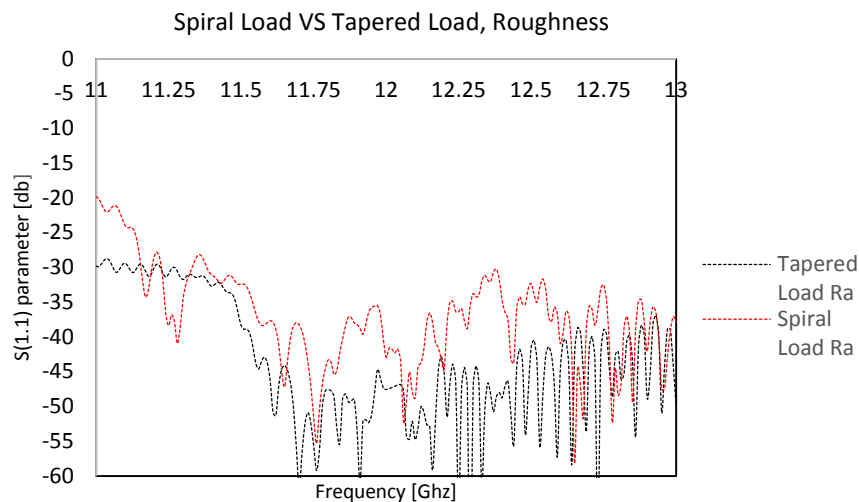


Figure 4.1.6. S_{11} parameter comparison between spiral and tapered load, HFSS, Roughness

First results are satisfactory is now needed to develop furtherly this model.

4.2 Vacuum pumping holes

Holes. As said before a vacuum pumping network is needed for our load, always considering that the main vacuum pump is placed in the centre of the spiral. The best option to make the vacuum pump communicate with all the internal volume is to create a series of holes in the load walls. These holes would surely modify the RF properties of the load, so the position of holes is fundamental.

The very beginning of the load is a crucial point, in case of high reflection at this point a big portion of the batch of waves would be lost and compromise the performance of the load. Has also to be taken into account that the number and the radius of the holes cannot be the same all along the waveguide, in fact dimensions of the spiral decrease along the path. For example, the first radius is 60.591mm, chosen n holes with a diameter of 1mm would be impossible to place them in the first radius of the spiral that is just 10mm.

A hole also introduces a wave scattering through the waveguide, this effect is well described by the scattering parameter which, as mentioned in Chapter 2, is a complex number. This complex number would change modulus and phase along the waveguide, nevertheless the modulus is in first approximation considered constant for the initial portion of the load. Choosing the position of the holes in the very beginning in a way that the scattering contribution of all these holes has sum 0 would lead to have no initial reflection, for this reason holes are settled at a distance of $\lambda/4$. Following this choice, initial reflection would vanish because, considering steps of $\lambda/4$, the scattering parameters would have same modulus but opposite sign. However it is worth to underline that this trick is particularly useful only in the initial part of the load. The overall effect is more complicated, because the modulus of the scattering parameter is not constant all along the waveguide. Nevertheless avoiding a high reflection in the very beginning of the load would be a good result, since also the RF power decreases in the final part of the load and consequently also the reflections from the holes[25].

For reasons stated above, 50 holes of 0.5mm radius each two semicircles are inserted with a distance of 7.1 degrees in the corresponding tapered part of the spiral, and 24 holes of 0.75mm radius with a distance of 7.1 degrees in the corresponding straight part.

In Fig. 4.2.1 the shape of the spiral load with holes is shown, as usual this picture corresponds to the vacuum, internal, part of the load, so holes will be visualized, in terms of vacuum, as cylinders.

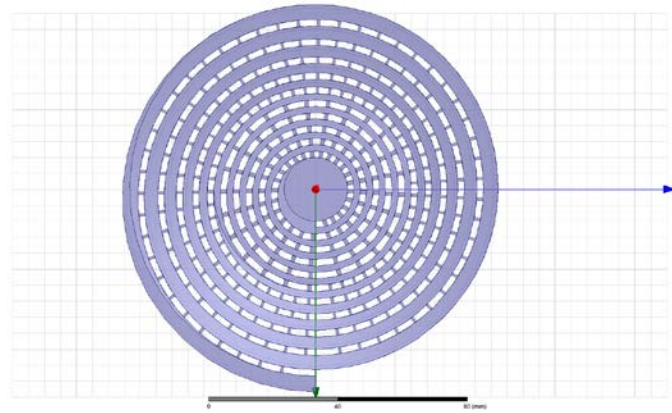


Figure 4.2.1 *Spiral with holes top-view*

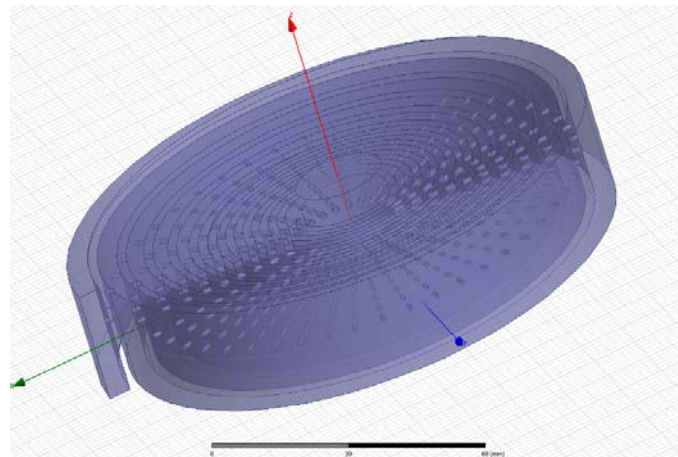


Figure 4.2.2 *Spiral with holes side-view*

At this point holes edges have to be rounded to avoid electromagnetic field enhancement and overheating. In fact at the edge of the holes without any rounding there is a discontinuity point of Maxwell's equation, and if equations are solved in this points would result an infinite electric and magnetic field with a corresponding infinite temperature.

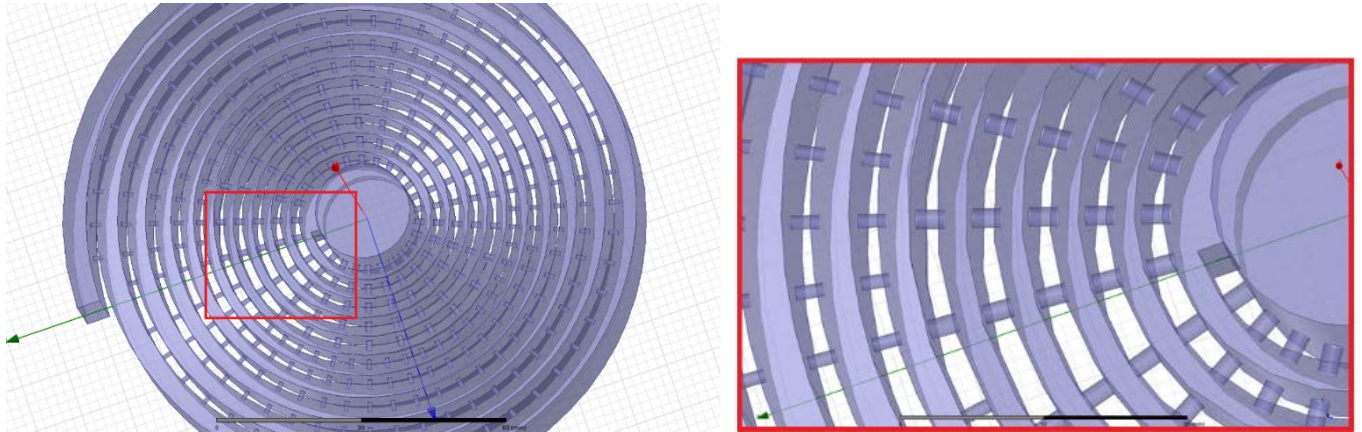


Figure 4.2.3. Spiral with holes, on the right detail zoom before rounding

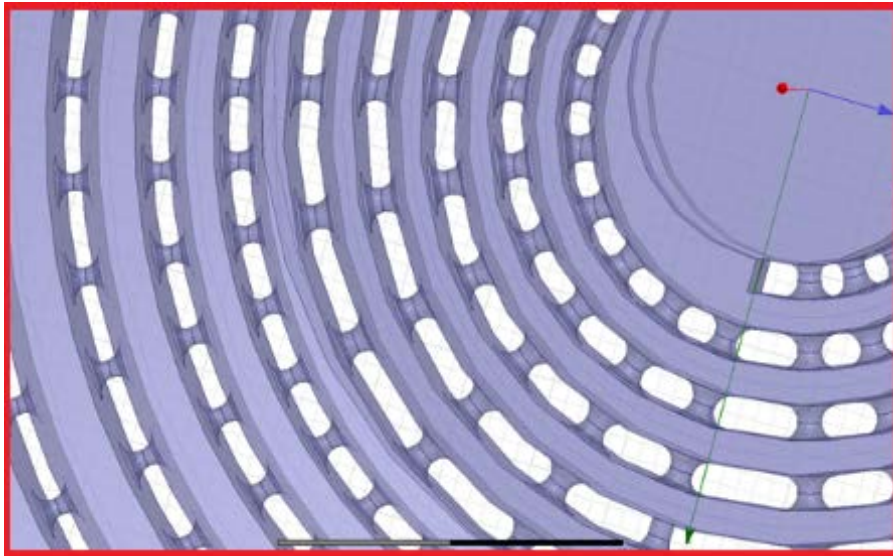


Figure 4.2.4. Spiral with holes, detail zoom after rounding

Simulations for this model are reported below,

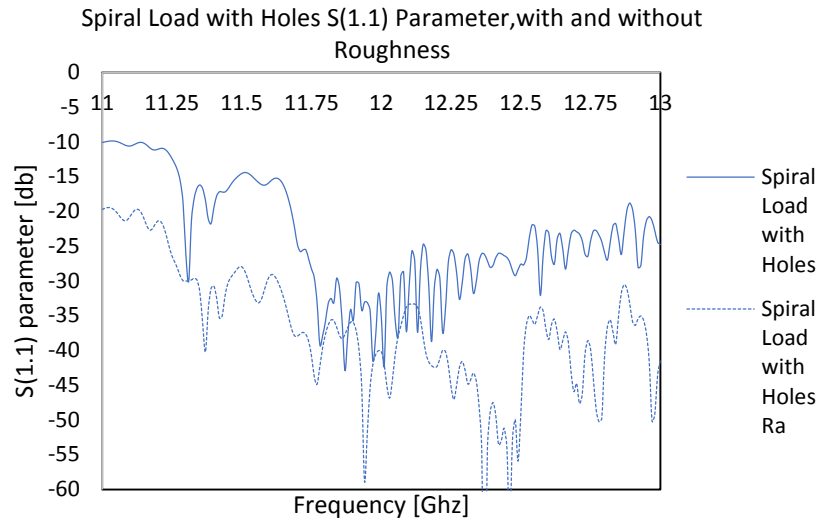


Figure 4.2.5. S_{11} parameter plot for spiral load with holes, with and without Roughness

Adding holes is noticeable that even without Roughness the required reflection of -30db reduction is reached. A comparison with previous models is reported below.

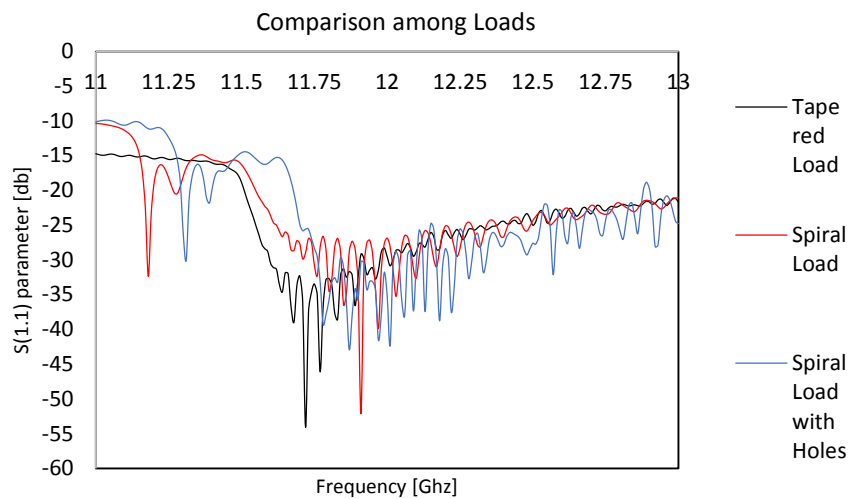


Figure 4.2.6. S_{11} values comparison between three previous models, no Roughness

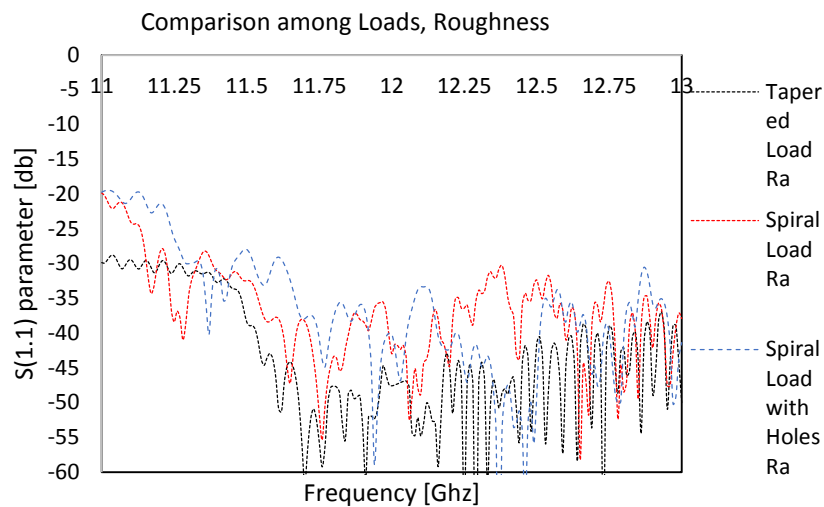


Figure 4.2.7. S_{11} values comparison between three previous models, Roughness.

It is interesting to notice a difference between the Spiral Load and the Spiral Load with holes in Fig.4.2.6. There is a difference between the absolute value of the scattering parameter, but there is also a global shift of the points that can be visualized.

Playing with holes or dimensions of the waveguide is possible to reduce or increase this shift according to needs, however for this model in a good range of points near the main 12 GHz frequency scattering parameter keeps a value of -30db.

4.3 Input waveguide transition

Introduction. Is now needed an input for the Load with different input dimensions in comparison with the ones of the last spiral model. This is due to the fact that the load will be connected to the accelerator through a standard dimensions flange $a=22.86\text{mm}$ $b=10.16\text{mm}$ (WR90).

This problem has not been considered before because this input box does not affect the scattering parameter of the Load (it's basically a waveguide) if the S_{11} of the input is low, the problem at this point is to choose the length of this input transition in order to have the lowest total reflection (S_{11})[26].

This input is obviously a tapered waveguide since it has the role to taper from the dimensions of the flange to the dimensions for our Load.

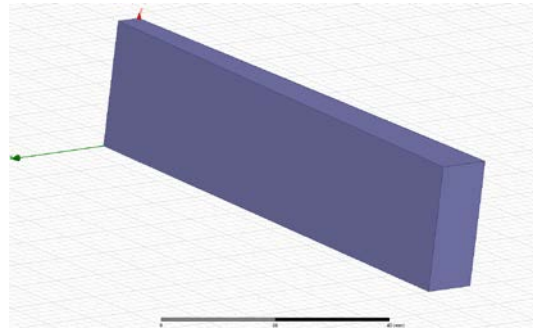


Figure4.3.1. Input waveguide..

A frequency sweep for different length of the box is created in order to choose the one with best reduction for a fixed 12 GHz frequency, we obtain:

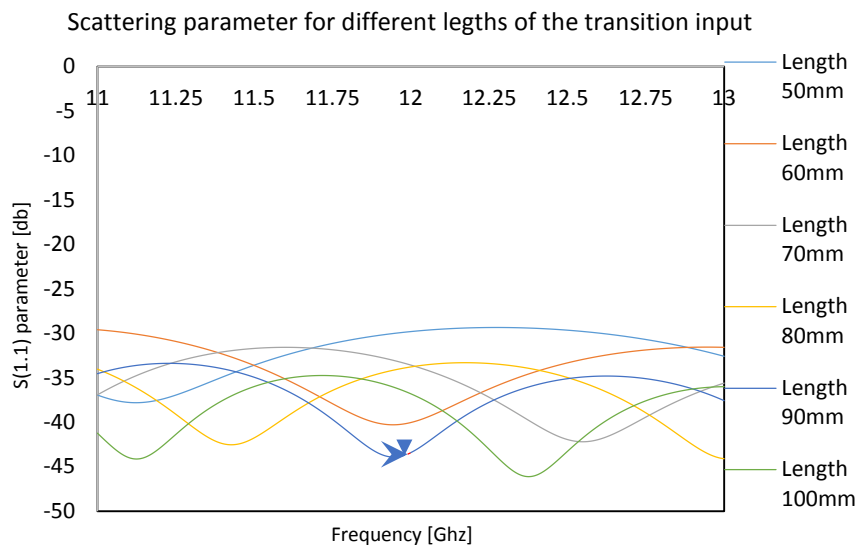


Figure4.3.2. S_{11} parameter for different lengths of the input.

The best reduction comes for 90mm length, an input transition of this length is then joined to the previous load model leading to the final RF design.

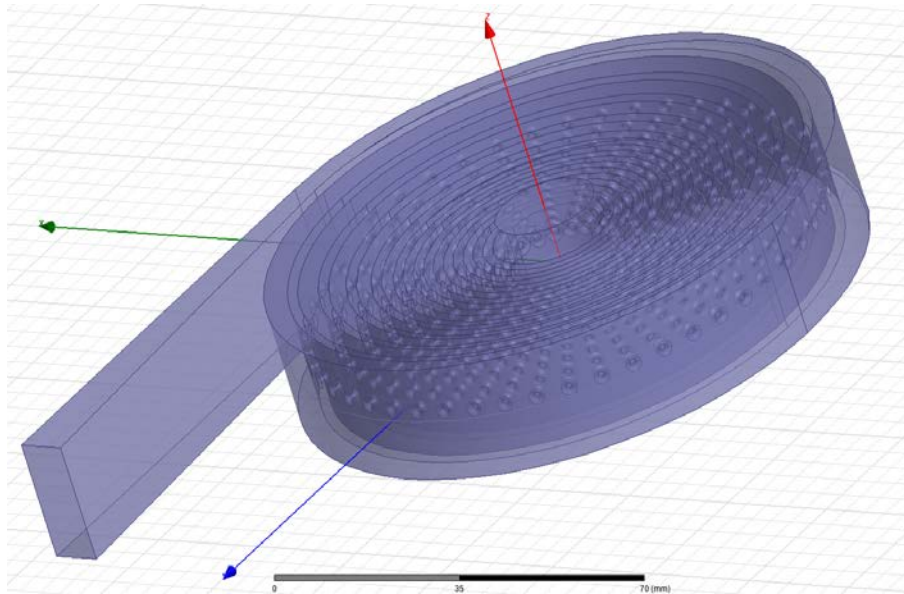


Figure4.3.3. Spiral with input side-view.

Simulations are reported below,

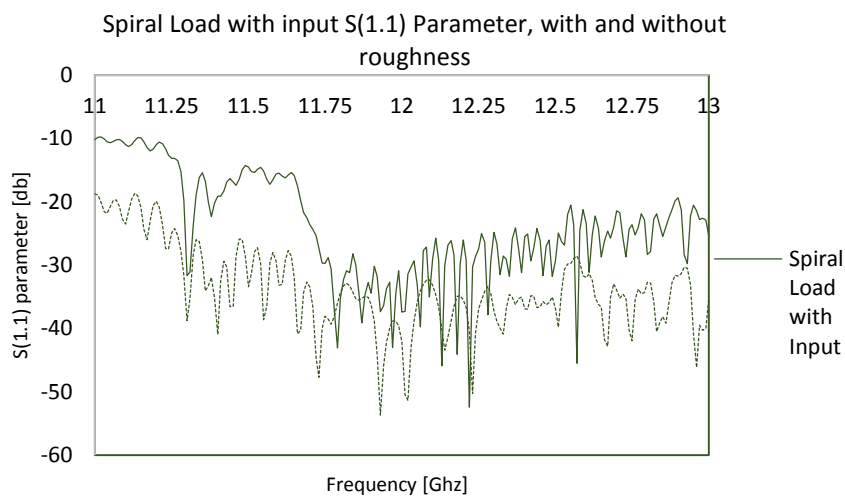


Figure4.3.4. S_{11} parameter plot for spiral load with input, with and without Roughness

For comparison not all data are joined since too many models have already been studied, is then preferable to compare this last model with the Spiral Load with Holes only.

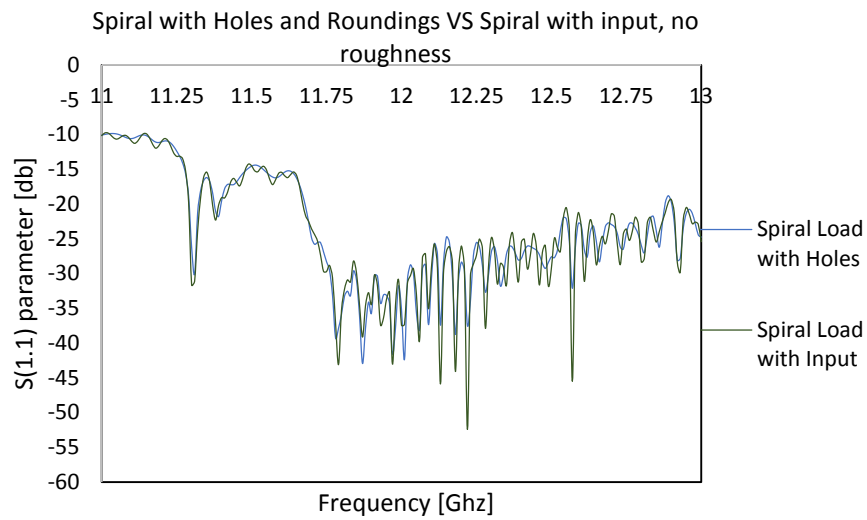


Figure 4.3.5. S_{11} parameter comparison plot for Spiral with holes and spiral with input, no Roughness

As expected there are no significant changes for the data without roughness.

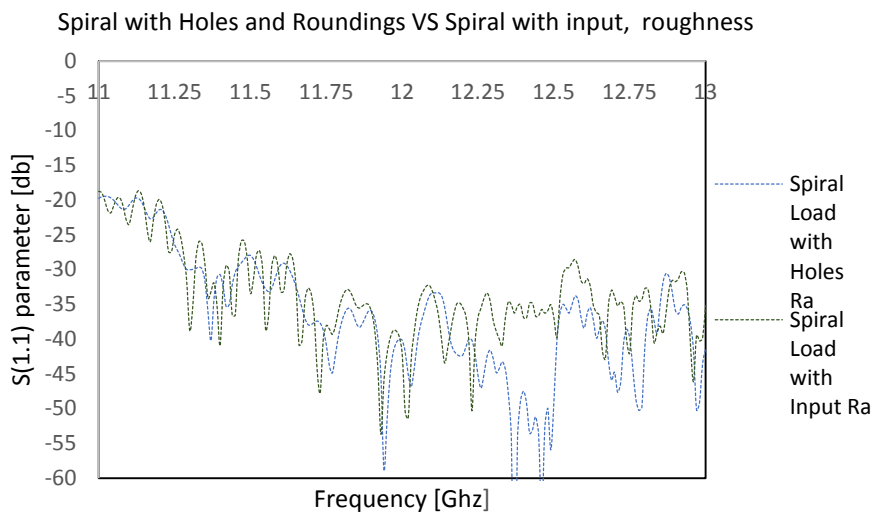


Figure 4.3.6. S_{11} parameter comparison plot for Spiral with holes and spiral with input, Roughness

4.4 Considerations

Considerations. The final model reaches a reduction of -30dB without considering roughness and -40dB with roughness according to simulations. These results can be considered satisfactory also taking into account that a vacuum pumping network has been inserted and the edges of the holes has been rounded.

The configuration of holes can as well considered efficient, thus the intuitive discussion about the annulation of the scattering parameter for a given positioning is proved to be right. Considering that the diameter of this load is approximately 14 cm instead of the 2.1 meters of the tapered load these results can be considered exceptionally good.

This page intentionally left blank

Chapter 5

Thermal simulations

5.1 RF Power

RF Power loss density. In Fig. 5.1.1 the density of the surface power loss due to the joule effect is shown. This plot is calculated in HFSS for an input power of 1 W.

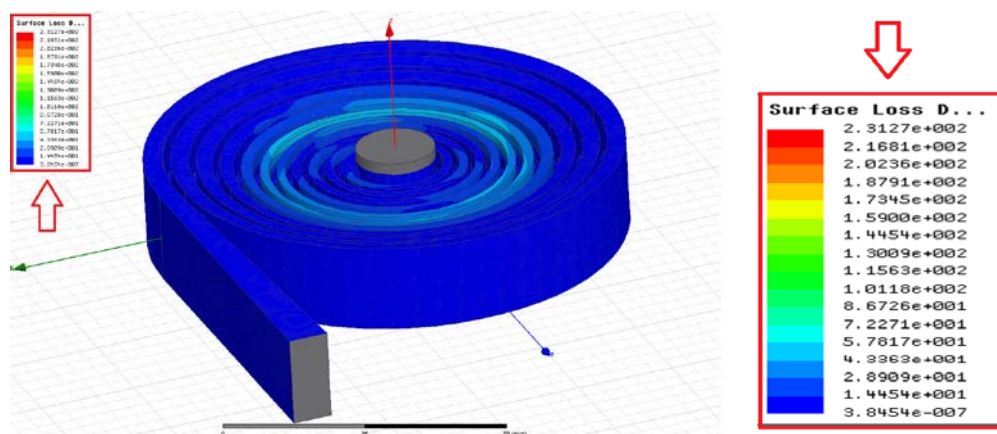


Figure 5.1.1. Power loss density (W/m^2).

Can be seen that in the transition between the tapered part and the straight part of the waveguide is present a higher density due to change of dimensions

Introduction to the problem. The load is projected to dissipate microwaves from any RF device, for example accelerating structures (AS)[27] or Klystrons[28].

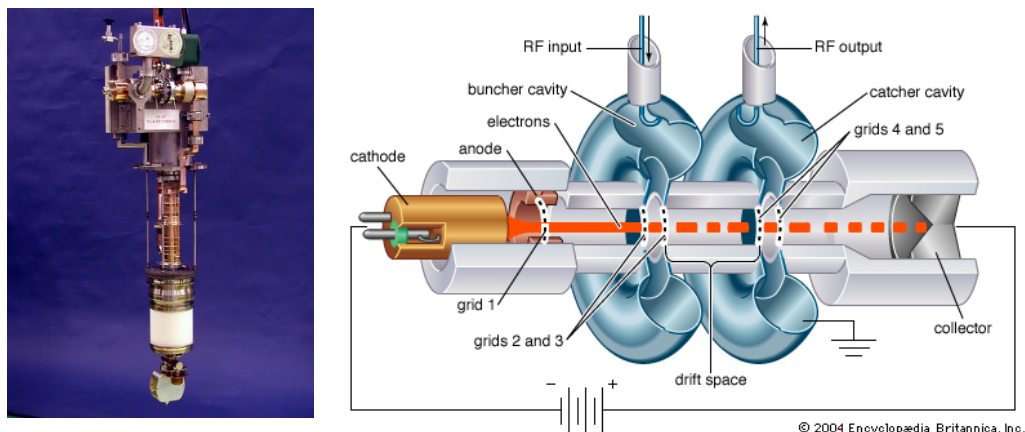


Figure 5.1.2. Klystron on the left, Klystron scheme on the right.

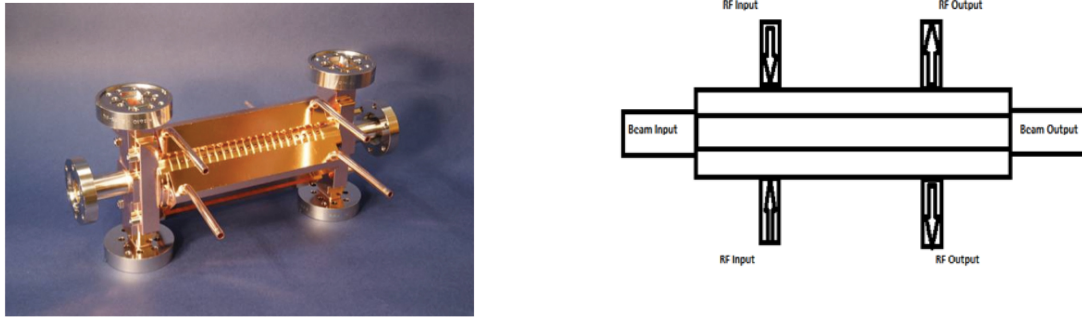


Figure 5.1.3. CLIC AS prototype on the left, AS scheme on the right

As can be seen from the schemes, the Klystron has only one high power RF port output (RF output) besides the CLIC AS has two out-put ports. This means that in order to dissipate the out-put power one load is needed for the Klystron and two for the AS. Actually couplers or splitters for outputs can be used, but in this chapter only the case mentioned before is analysed, that is the most general one.

Average Power. The load at work receives a pulsed signal, with a “Peak” power (P_{pk}), given by the maximum power of the signal. An important quantity that can be defined is the average Power, this is the Power averaged over the period of the pulse T . In this contest the instantaneous power $p(t)$ is also a periodic function of period T . The *peak power* is simply defined by:

$$P_{pk} = \max(p(t)) \quad (5.1)$$

If the energy per pulse is defined as:

$$\epsilon_{pulse} = \int_0^T p(t) dt \quad (5.2)$$

then the average power is:

$$P_{av} = \int_0^T p(t) dt = \frac{\epsilon_{pulse}}{T} \quad (5.3)$$

The pulse length τ_p can be defined such that $P_{pk}\tau_p = \epsilon_{pulse}$ so that the ratios

$$\frac{P_{av}}{P_{pk}} = \frac{\tau_p}{T} \quad (5.4)$$

are equal. These ratios are called the *duty cycle* of the pulse train[29].

In our case a very instantaneous change of the Power that varies from the 0 value to the Peak Power is supposed, see Fig.5.1.4.

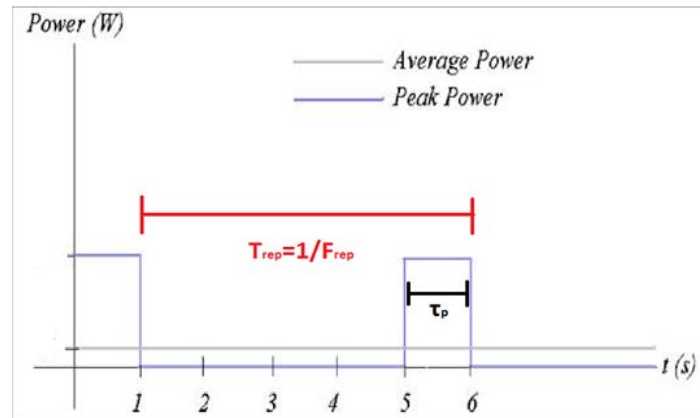


Figure 5.1.4. Average Power

Where F_{rep} is the repetition frequency and τ_p is the pulse length in time. With this assumption Eq. 5.4 becomes:

$$P_{av} = F_{rep} P_{pk} \tau_p \quad (5.5)$$

Is possible then to proceed in the calculation of the values for the average power of the Klystron and the AS, given values of P_{pk} , F_{rep} , τ_p [27], [28],

	Klystron		AS
P_{pk}	50 MW		16MW
F_{rep}	50Hz		50Hz
τ_p	1500ns		242ns

Table 5A. Specifics of Klystron and AS

Is found respectively:

$$P_{av,Klystron} = 3750W$$

$$P_{av,AS} = 193.6W$$

These are the average powers that the load is supposed to bear.

5.2. Model for Simulations.

Metal model. From this point thermal simulations study starts using the package Ansys Workbench. In order to implement the load model in this software a “metal” model is needed, this model is slightly different from the ones we used for simulations in HFSS (vacuum part). In fact this metal model would represent the load itself and not the vacuum part inside, is worth to be reminded that wall thickness required is 2mm. The model is produced in HFSS and then imported in ANSYS. For the metal specifics of Ti6Al4V are used, this is a titanium alloy that will be used for the fabrication, (see Appendix 2 for more details about Ti6Al4V)

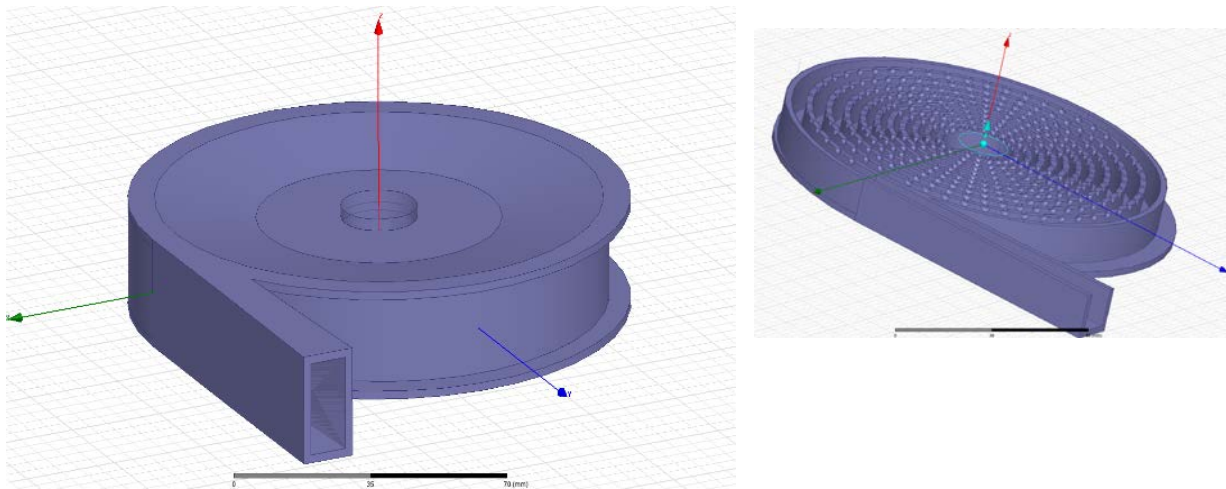


Figure 5.2.1. Metal model of the load on the left, symmetric cut in xy plane of the metal model on the right.

Cooling system. In order to proceed in simulations has first to be considered that the load has to be equipped with a cooling system. To create a spiral cooling system for the load the same process used to create the load is followed, thus first a spiral linear growing polyline is generated and afterwards walls of the cooling system are swept on this polyline. The chosen diameter is 0.75mm.

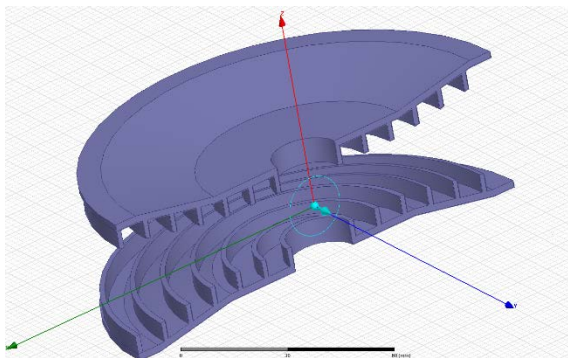


Figure 5.2.2. Cooling system, symmetric cut in the zy plane.

In the picture can be seen that the cross-section of the cooling channels are square so is not totally correct to use the word diameter in this context. However has also to be considered that roundings will be added at the walls' corners of the cooling channels and square cross section would become, in the end, a circular one. However will be seen furtherly in the chapter that in the context of simulations considering the cooling channels with square or circular cross-section does not make any difference, in fact what will be important is the hydraulic diameter of the cooling channels.

After building the cooling system in HFSS this is fixed to the load.

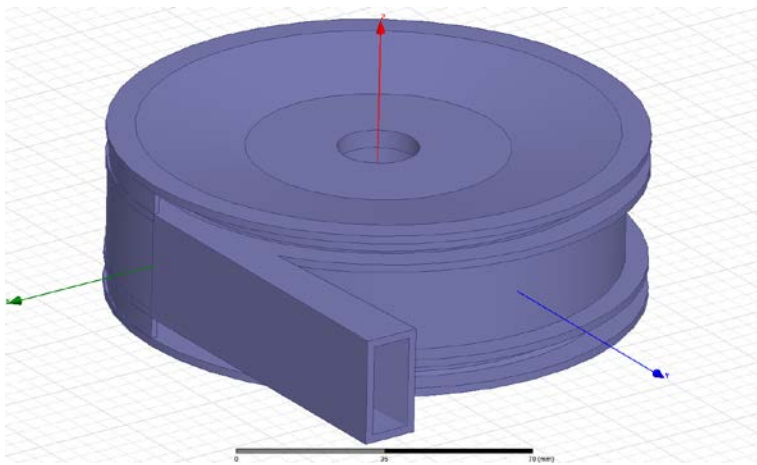


Figure5.2.3. Load with cooling system.

Final Considerations. Before starting simulations is needed to quantify the “cooling factor”. In fact the cooling mechanism of the load is implemented in ANSYS WORKBENCH with a water flow in the cooling channels. The cooling factor mainly depend on the cross section of the channels and on the flow velocity of water. To practically quantify this factor some heat transfer theory is needed.

5.3 Heat Transfer Theory.

Hydraulic diameter. The hydraulic diameter, D_H , is a commonly used term when handling flow in noncircular tubes and channels. Using this term one can calculate many things in the same way as for a round tube. It is defined as

$$D_H = \frac{4A}{P} \quad (5.6)$$

Where A is the cross sectional area and P is the wetted perimeter of the cross-section[30]. For a pipe with square cross section and with length a :

$$D_H = a$$

Convection coefficient. Convection is the mechanism of heat transfer through a fluid in the presence of bulk fluid-motion. Convection is classified as natural (or free) and forced convection depending on how the fluid motion is initiated. In natural convection, any fluid motion is caused by natural means such as the buoyancy effect, i.e. the rise of warmer fluid and fall the cooler fluid. Whereas in forced convection, the fluid is forced to flow over a surface or in a tube by external means such as a pump or fan (this will be the only case we will study and corresponds to our case). Convection heat transfer is complicated since it involves fluid motion as well as heat conduction. The fluid motion enhances heat transfer (the higher the velocity the higher the heat transfer rate). The rate of convection heat transfer is expressed by Newton's law of cooling:

$$\dot{q} = h(T_s - T_f) \quad (5.7)$$

$$\dot{Q} = hA(T_s - T_f) \quad (5.8)$$

Where T_s is the temperature of the surface, T_f the temperature of the fluid, A is the transfer surface area and h is the convection coefficient.

As mentioned before the convection coefficient h strongly depends on the fluid properties and , and the type of the fluid flow (laminar or turbulent).

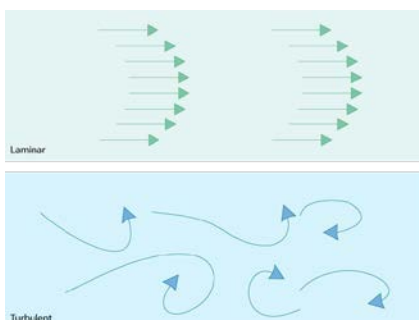


Figure 5.3.1. Laminar and turbulent flow.

Without giving more details on turbulent and laminar flows an intuitive idea is presented in Fig.5.2.0. It is noticeable that a laminar flow is characterized by parallel flux lines and a turbulent flow by a chaotic manner for flux lines.

Consider now a fluid flowing along a plate (Solid hot surface in Fig5.3.2).

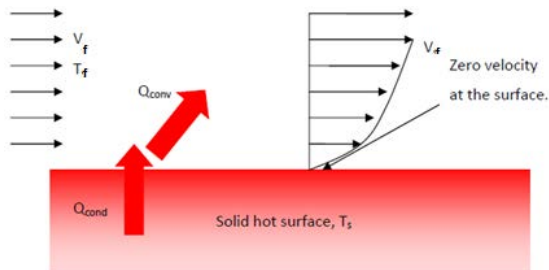


Figure 5.3.2. Flow along a plate.

It is assumed that the velocity of the fluid is zero at the wall, this assumption is called *noslip*-condition. As a result, the heat transfer from the solid surface to the fluid layer adjacent to the surface is by pure conduction, since the fluid is motionless. Thus,

$$\dot{q} = -k_{fluid} \left(\frac{\partial T}{\partial y} \right)_{y=0} \quad \rightarrow \quad h = \frac{-k_{fluid} \left(\frac{\partial T}{\partial y} \right)_{y=0}}{(T_s - T_f)} \quad (5.9)$$

$$\dot{q} = h(T_s - T_f)$$

The convection coefficient, in general, varies along the flow direction. The mean or average convection coefficient for a surface is determined by (properly) averaging the local heat transfer coefficient over the entire surface [31].

Non dimensional Groups. In convection, it is a common practice to non-dimensionalize the governing equations and combine the variables which group together into dimensionless numbers (groups).

Nusselt number: non-dimensional heat transfer coefficient

$$Nu = \frac{hD_h}{k} \quad (5.10)$$

where D_h is the hydraulic diameter.

Nusselt number represents the enhancement of heat transfer through a fluid as a result of convection relative to conduction across the same fluid layer.

Reynolds number: ratio of inertia forces to viscous forces in the fluid

$$Re = \frac{vD_h}{\nu} \quad (5.11)$$

At large Re numbers, the inertia forces, which are proportional to the density and the velocity of the fluid, are large relative to the viscous forces; thus the viscous forces cannot prevent the random and rapid fluctuations of the fluid (turbulent regime).

The Reynolds number at which the flow becomes turbulent is called the critical *Reynolds Number*. For a pipe (cooling ducts) the critical Re is experimentally determined to be approximately, $Re_{critical} = 4 \times 10^3$

Prandtl number: is a measure of relative thickness of the velocity and thermal boundary Layer

$$Pr = \frac{\mu C_p}{k} \quad (5.12)$$

For previous relations:

mass density : ρ , (kg/m^3)

specific heat capacity : C_p ($J/kg \cdot C$)

dynamic viscosity : μ , ($N \cdot s/m^2$)

kinematic viscosity : ν , μ / ρ (m^2/s)

thermal conductivity : k , ($W/m \cdot C$)

Nusselt's correlation. In the very beginning was said that when a liquid flows along a surface (plate, pipes etc...) the convection coefficient is not constant and the velocity and also the behaviour of the fluid (turbulent or laminar flow) are difficult to be predicted. However for a flux in a pipe can be reached the so called condition of fully developed flow. When the flow is fully developed the convection coefficient stays constant as the Nusselt number. The Nusselt number is related to the convection coefficient through equation 5.10 . Usually is possible, in fully developed flow, to obtain the Nusselt number from Prandtl's and Reynold's ones. The most general correlation is given by the formula:

$$Nu = C Pr^n Re^m \quad (5.13)$$

Where C,n,m are constants that vary according to the specific physical problem considered . In case of a square or circular duct, Nusselt's correlation for laminar flow takes the form of:

$$Nu = 1.86 \left(\frac{RePr}{L/D_h} \right)^{1/3} \quad (5.14)$$

This formula is also called Seider and Tate equation and L represents the total length of the pipe while D is the hydraulic diameter,

for turbulent flow in case of square or circular duct:

$$Nu = 0.023 Pr^{0.3} Re^{0.8} \quad (5.15)$$

Also called Dittus-Bolter equation[32]. Equations for Nusselt's correlation are determined experimentally and many variants can be used instead of these correlations, these specific ones are used due to good results obtained by previous applications.

5.3 Application of Heat Transfer Theory

Heat coefficient calculation. Eqs 5.14, 5.15, can be combined with 5.10 to calculate the convection coefficient for water flow in the cooling system.

Fixed the hydraulic diameter in the pipe, and the liquid properties (water in our case) the convection coefficient would be function of the velocity only.

Was seen before that given Reynold's number is possible to understand if the flow is laminar or turbulent. For a circular or rectangular pipe the value $Re=4000$ is commonly used as a Reynold's critical number.

For this value of Re , given only one velocity, two different values of the convection coefficient are calculated. One in the hypothesis the flow is laminar and one in the hypothesis the flow is turbulent. Data are reported below with the plot of the convection coefficient in function of the velocity.

v (m/s)	Re		Nu		h (W/(m ²)C)
0.01	83		2.16		173
0.47	3940		7.79		623
v (m/s)	Re		Nu		h (W/(m ²)C)
0.47	3940		38		3040
1	8370		69.43		5554
3.52	29500		190.22		15217

Table 5B. List of convection coefficient for the cooling system.

in Fig 5.3.3 the discontinuity for the value $v=0.47\text{m/s}$ can be clearly seen .

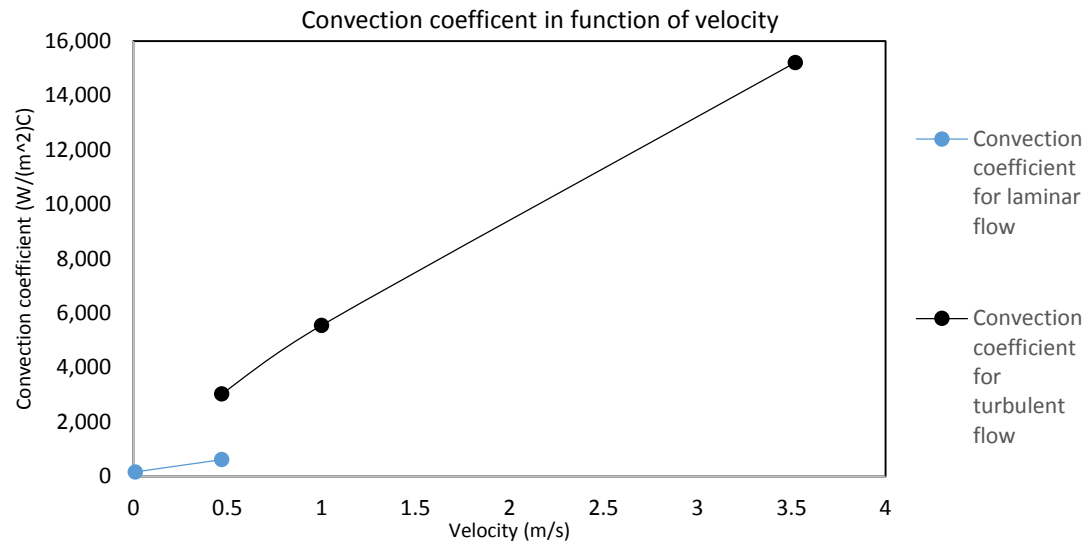


Figure5.3.3. Convection coefficient of the cooling system in function of velocity.

ANSYS WORKBENCH. These values of convection coefficient are then implemented in ANSYS for thermal simulations. The convection coefficient is applied on the surface of the load that will be wetted by the fluid. It is now needed to set different values of the input power for the load.

5 power values are chosen in the range from the lowest expectation power (given by the AS) to the highest expectation power, given by the klystron. Three different fields' responses of the load are then studied: the response in temperature (temperature field quantified in C), the response in deformation (deformation field quantified in mm) and the response in stress (stress field quantified in Gpa). These responses obviously vary according to the convection coefficient applied on our surface, so it is needed to calculate these fields for different values of h . Are here reported plots for each convection coefficient but data only for the highest value.

Temperature field.

Below the temperature distribution on the surface of the load for a value of the h coefficient: $h=623 \text{ W}/(\text{m}^2)\text{C}$ and an input power: $P=1875\text{W}$ is reported.

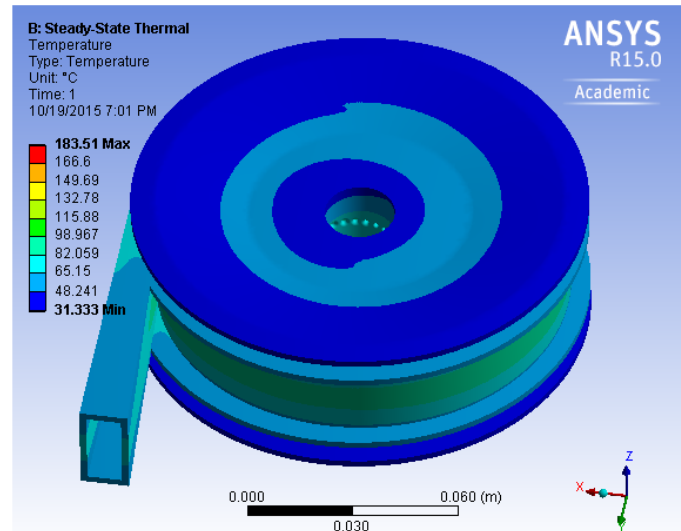


Figure5.3.4. Temperature field of the load..

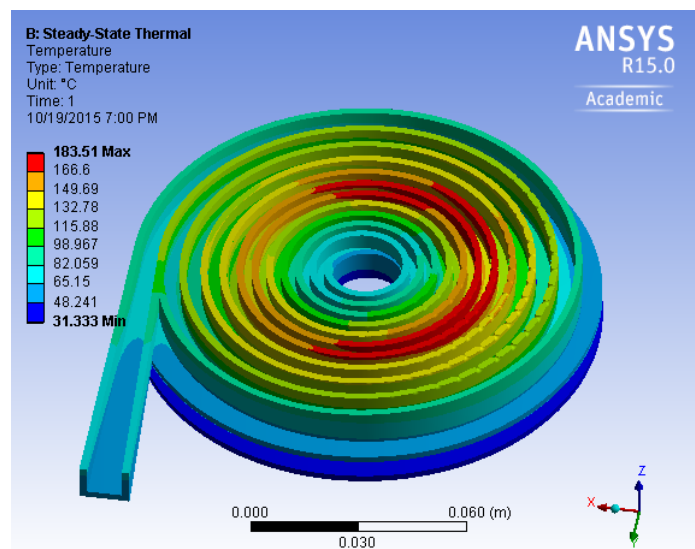


Figure5.3.5. Temperature field of the load cut in xy plane

As said in the beginning data reported below correspond to the maximum value of the convection coefficient.

$h=15217 \text{ W/m}^2\cdot\text{C}$				
$v=3.52\text{m/s}$				
POWER(W)	Tmax (C)	Tmin (C)		$\Delta T(\text{C})$
193.6	28.227	22		6.227
1034.3	55.266	22		33.266
1875	82.306	22.001		60.305
2812.5	112.46	22.001		90.459
3750	142.61	22.001		120.609

Table 5C. Temperature values for 15217 ($\text{W}/(\text{m}^2)\text{C}$) heat coefficient.

The plot of the difference between maximum and minimum temperature, ΔT in function of power for different convection coefficient is reported below.

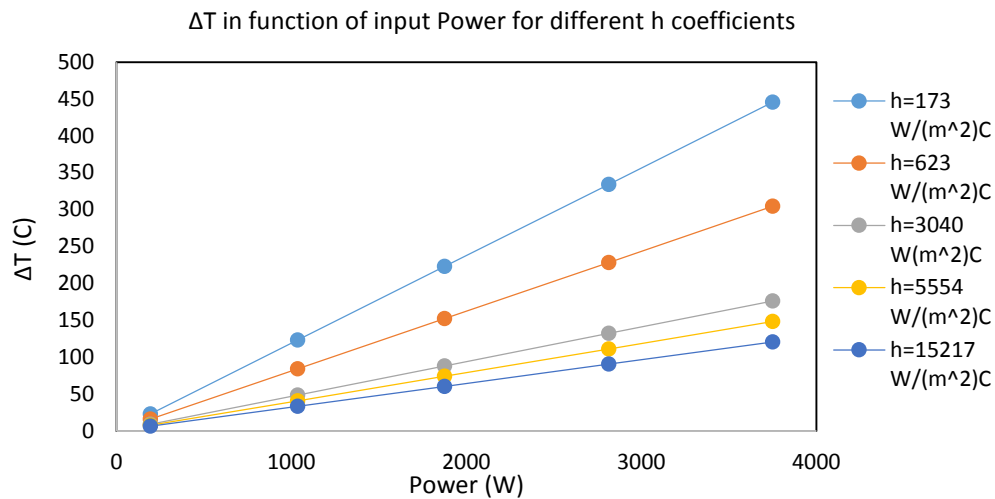


Figure 5.3.3. ΔT in function of input Power for different h coefficients.

Can be seen from the table and from the plot that for the AS structure power (193.6 W) the difference in temperature is negligible, but for the Klystron power this difference is more than 100 degree C. Nevertheless has to be considered that a high delta T is not a problem if it the load deformation is low, so before judging the quality of the temperature response deformation has to be checked.

Deformation field.

The deformation is the difference (calculated in mm) between the dimensions of the load at zero power level and a nominal power level. In this case deformation is caused by the heat distribution on the material.

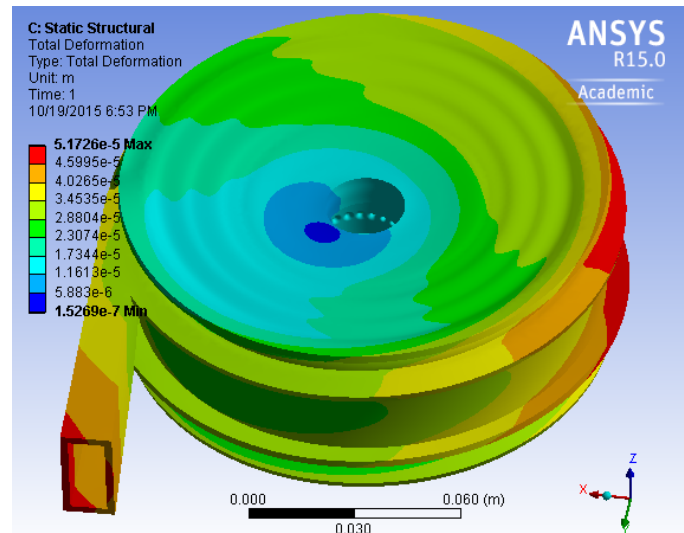


Figure5.3.4. Deformation field of the load.

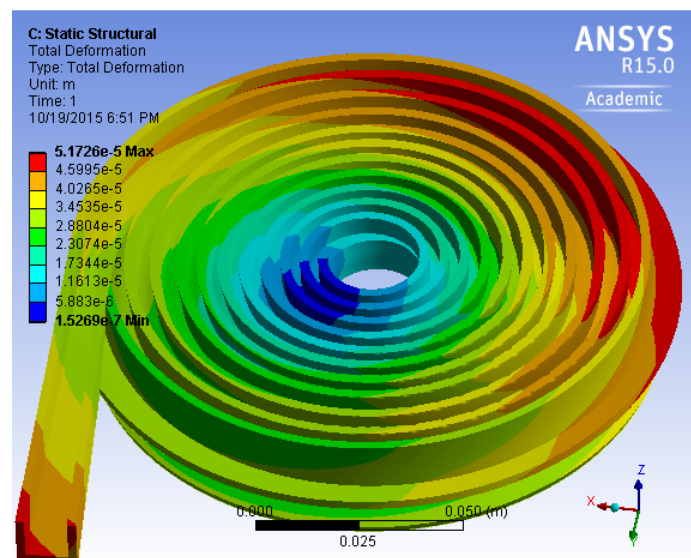


Figure5.3.5. Deformation field of the load, cut in xy plane

Data reported below correspond to the maximum value of the convection coefficient.

h=15217 W/(m ²)C				
v=3.52 m/s				
Power(W)	Dmax(mm)	Dmin(mm)		ΔD (mm)
193.6	0.00195	0.0000282		0.00192
1034.3	0.0104	0.000151		0.0102
1875	0.0188	0.000273		0.0186
2812.5	0.0283	0.00041		0.0278
3750	0.0377	0.000547		0.0371

Table 5D. maximum Deformation values for 15217 (W/(m²)C) heat coefficient.

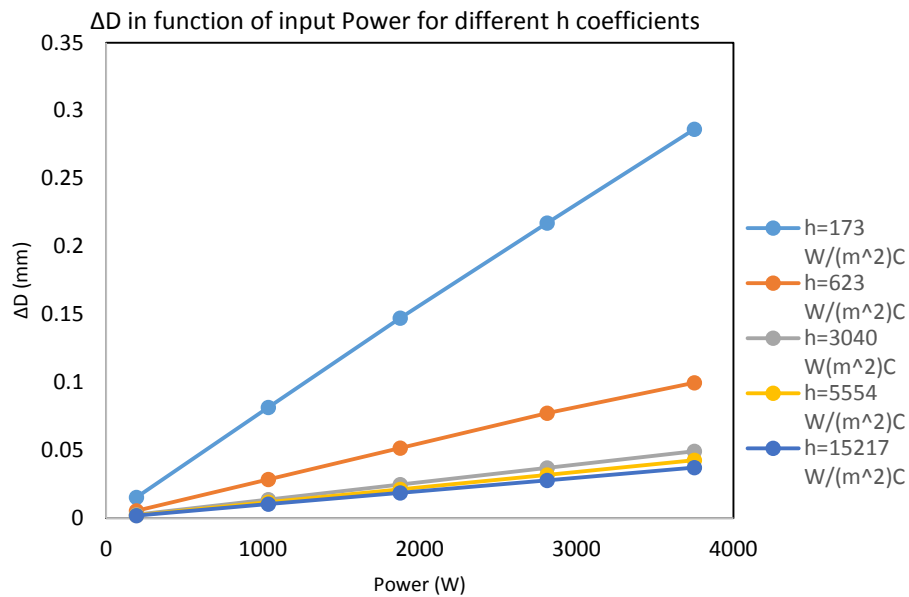


Figure 5.3.6. ΔD in function of input Power for different h coefficients.

Can be see than even using the maximum power, 3750W (power of the Klystron), the deformation is small compared to the dimensions of the load[33].

STRESS FIELD.

Are reported below results representing the pressure that the load will have to bear during the beam propagation.

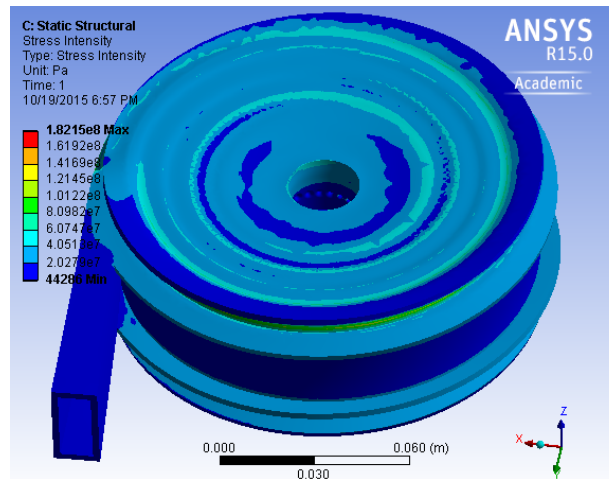


Figure5.3.7. Stress field of the load

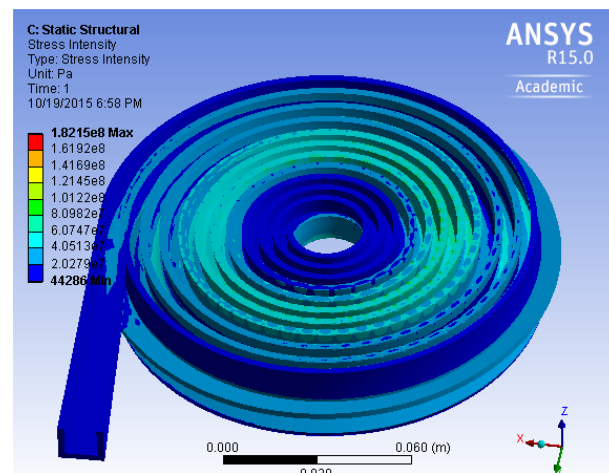


Figure5.3.8. Stress field of the load, xy plane cut.

Data for $h=15217 \text{ W}/(\text{m}^2)\text{C}$ are reported below,

$h=15217 \text{ W}/(\text{m}^2)\text{C}$				
$v=3.52 \text{ m/s}$				
Power (W)	$S_{\text{max}}(\text{Gpa})$	$S_{\text{min}}(\text{Gpa})$		ΔS (GPa)
193.6	1.03E-02	0.000541		9.76E-03
1034.3	5.48E-02	2.89E-05		5.48E-02
1875	9.93E-02	5.24E-05		9.92E-02
2812.5	1.49E-01	7.86E-05		1.49E-01
3750	1.99E-01	0.000105		1.99E-01

Table 5E. Stress values for 15217 ($\text{W}/(\text{m}^2)\text{C}$) heat coefficient.

Below plot the difference between maximum and minimum stress, ΔS as a function of power for different convection coefficients.

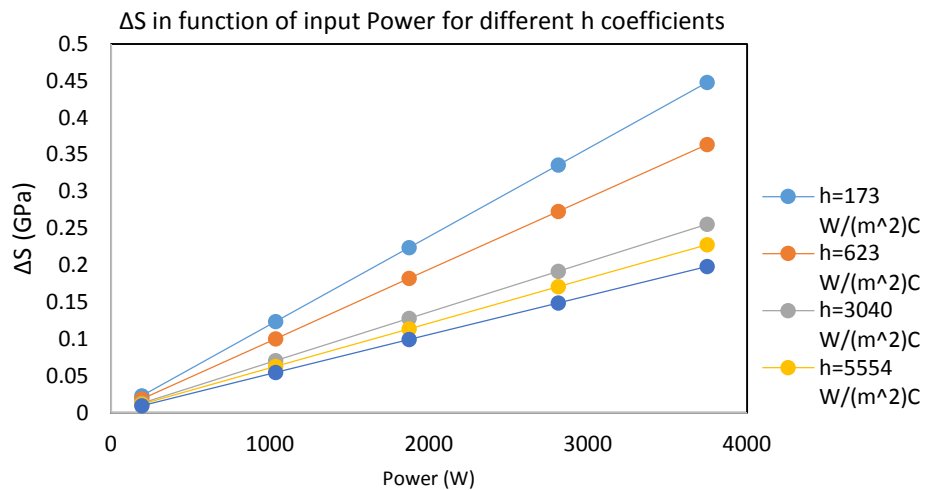


Figure 5.3.9. ΔS in function of input Power for different h coefficients.

In order to understand if this results are satisfactory or not we have to consider the yield strength of the Ti6Al4V alloy.

Yield strength. A yield strength or yield point of a material is defined in engineering and materials science as the stress at which a material begins to deform plastically[34]. Prior to the yield point the material will deform elastically and will return to its original shape when the applied stress is removed. Once the yield point is passed, some fraction of the deformation will be permanent and non-reversible. The yield strength for Ti6Al4V alloy is estimated to be approximately 0.9 Gpa, according to simulations this value is never reached.

5.4 Pressure

Pressure drop. The pressure drop needed to sustain an internal flow in the cooling system is now analysed. This parameter determines pump or fan power requirements.

To determine the pressure drop, it is convenient to work with the Moody friction factor, which is a dimensionless parameter defined as

$$f = \frac{-(\frac{dp}{dx})D}{\rho \frac{v_m^2}{2}} \quad (5.16)$$

Where p is the pressure D the hydraulic diameter ρ the density and v_m the average velocity of the flow.

This factor in case of laminar flow takes the simple form:

$$f = 64/Re \quad (5.17)$$

And for turbulent flow:

$$f = \sqrt{(0.79 \ln Re - 1.64)} \quad (5.18)$$

Note that f , hence dp/dx , is a constant in the fully developed flow region. Using eq.5.16 the pressure drop $\Delta p = p_1 - p_2$ associated with fully developed flow from the axial position x_1 to x_2 may be expressed as:

$$\Delta p = \int_{p_1}^{p_2} dp = f \frac{\rho v_m^2}{2D} \int_{x_1}^{x_2} dx = f \frac{\rho v_m^2}{2D} (x_2 - x_1) \quad (5.19)$$

Where v_m is the mean velocity of the flow [35].

Pressure drop of the cooling system. Is then calculated the pressure drop at the edges of the cooling system substituting to $(x_2 - x_1)$ the quantity L (length of the cooling system). Pressure drop is then estimated for different velocities. Data are reported below,

Laminar flow				
v (m/s)	f			Δp (bar)
0.01	0.68			0.0001
0.47	0.0144			0.0049
Turbulent flow				
v (m/s)	f			Δp (bar)
0.47	0.0416			0.0143
1	0.0331			0.0516
3.52	0.0237			0.458

Table 5F. List of pressure drops in function of velocities for the cooling system.

Results can be reported on logarithmic scale as below:

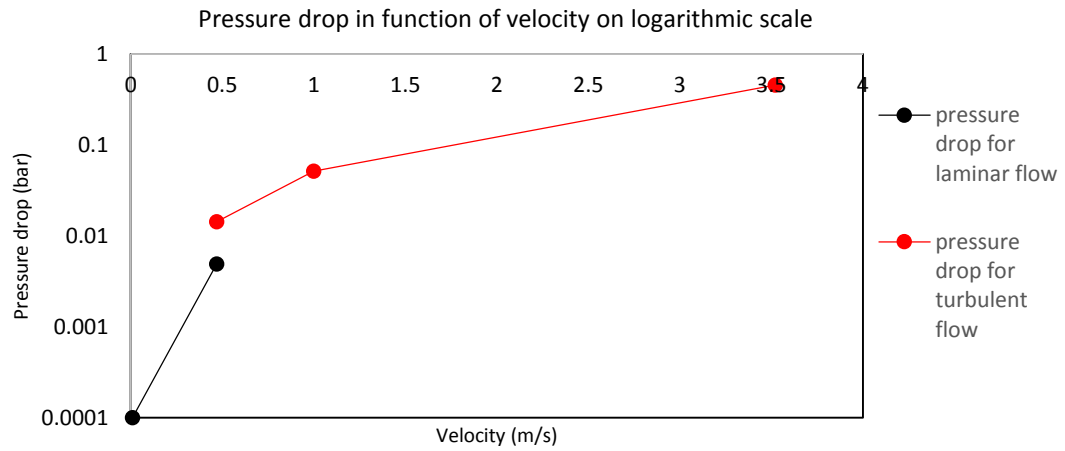


Figure 5.4.1. Pressure drop in function of velocity on logarithmic scale

the pump commonly used for cooling channels provides a pressure above 1 bar which is higher than the analytical values found.

This page intentionally left blank

6-RF check

6.1 CATIA model

“**Realistic Model**”. The final load model studied in Chapter 4 is not yet the final model for fabrication. A “realistic” model, based on the one generated in HFSS, has afterwards been developed by a mechanical engineer in CATIA interactive environment. Below the CATIA model is shown:

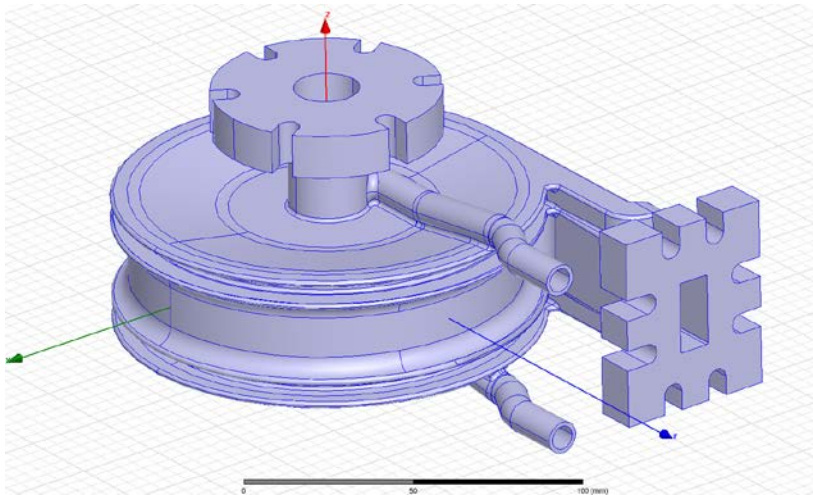


Figure 6.1.1. CATIA model of the load

As can be seen in Fig.6.1.1 connectors-flanges have been added and the external surfaces has been rounded in order to avoid stress enhancement, finally also two input pipes for the cooling system have been fixed at the load. Regarding the internal part is visible (see Fig.6.1.2) that the edges of the internal spiral have been rounded as well.

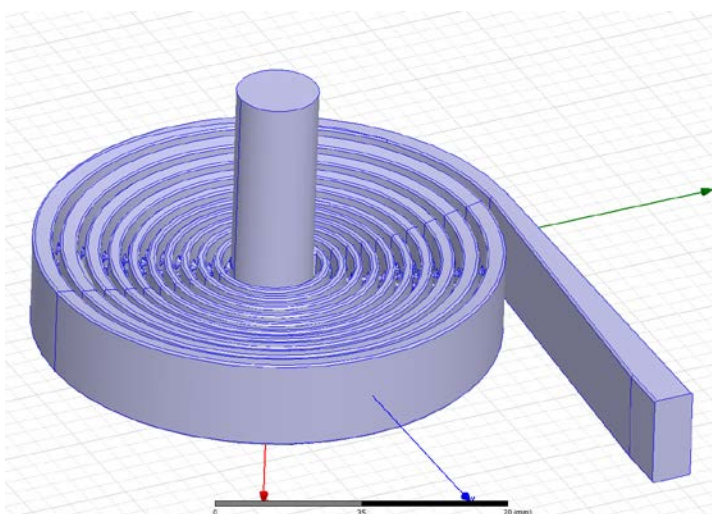


Figure 6.1.2. CATIA model internal part

In order to check that the RF properties of the project designed in CATIA are the same as of the original HFSS design an RF check is done,

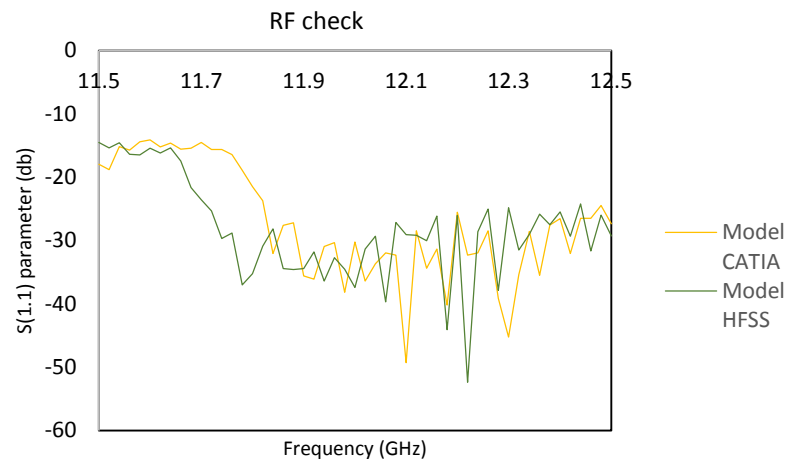


Figure 6.1.3. RF check

Can be seen that even though there is a global shift of the scattering parameter the requested reflection -30dB is reached.

This page intentionally left blank

CONCLUSIONS

The RF model of the compact load has been extensively studied. RF simulations that give a -30 dB reduction factor for the final model are satisfactory. In addition, was also seen that deformation and pressure don't exceed required values, as well as the pumping power for the water cooling system is adequate to the one typically used.

In last chapter that the CATIA model has been analysed showing again that RF properties don't change for the working frequency of 12 GHz. This very last model created in CATIA is the final model that have already been sent for prototype fabrication.

Prototype measurements could not be added to the present document for a time matter, in fact this document is being written while the prototype is still being fabricated.

The compact load developed has been shown to be a valid model and might be used in future as a fundamental component of the next linear accelerator CLIC.

APPENDIXES

A-3D printing technology

3D printing, also known as additive manufacturing, is any of various processes used to synthesize a three-dimensional object. In 3D printing, successive layers of material are laid down under computer control. These objects can be of almost any shape or geometry, and are produced from a 3D model or other electronic data source. A 3D printer is a type of industrial robot [23].

SELECTIVE LASER SINTERING. *An additive manufacturing layer technology, SLS involves the use of a high power laser (for example, a carbon dioxide laser) to fuse small particles of plastic, metal, ceramic, or glass powders into a mass that has a desired three-dimensional shape. The laser selectively fuses powdered material by scanning cross-sections generated from a 3-D digital description of the part (for example from a CAD file or scan data) on the surface of a powder bed. After each cross-section is scanned, the powder bed is lowered by one layer thickness, a new layer of material is applied on top, and the process is repeated until the part is completed.*

Because finished part density depends on peak laser power, rather than laser duration, a SLS machine typically uses a pulsed laser. The SLS machine preheats the bulk powder material in the powder bed somewhat below its melting point, to make it easier for the laser to raise the temperature of the selected regions the rest of the way to the melting point[24].

Unlike some other additive manufacturing processes, such as stereo-lithography (SLA) and fused deposition modeling (FDM), SLS does not require support structures because the part being constructed is surrounded by un-sintered powder at all times, this allows for the construction of previously impossible geometries.

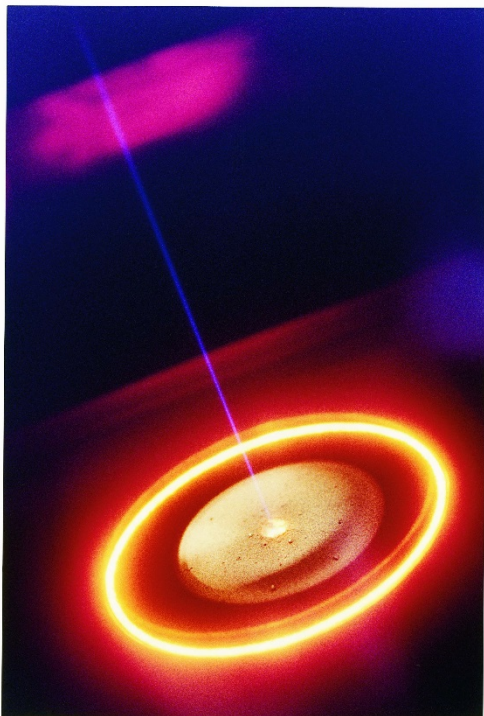
Since patents have started to expire, affordable home printers have become possible, but the heating process is still an obstacle, with a power consumption of up to 5 kW and temperatures having to be controlled within 2 °C for the three stages of preheating, melting and storing before removal[25].



FigureA.1. *Laser sintering 3D printer*

ELECTRON BEAM MELTING. *Metal powders can be sintered into a solid mass using an electron beam as the heat source. This is used as a 3D printing technique, similar to selective laser sintering. This is sometimes called "electron beam melting". EBM technology*

manufactures parts by melting metal powder layer by layer with an electron beam in a high vacuum. In contrast to sintering techniques, both EBM and SLM achieve full melting of the metal powder[26]. This solid freeform fabrication method produces fully dense metal parts directly from metal powder with characteristics of the target material. The EBM machine reads data from a 3D CAD model and lays down successive layers of powdered material. These layers are melted together utilizing a computer controlled electron beam. In this way it builds up the parts. The process takes place under vacuum, which makes it suited to manufacture parts in reactive materials with a high affinity for oxygen, e.g. titanium[27]. The process is known to operate at higher temperatures (up to 1000 °C), which can lead to differences in phase formation through solidification and solid state phase transformation. The powder feedstock is typically pre-alloyed, as opposed to a mixture.. Compared to SLM and DMLS, EBM has a generally superior build rate because of its higher energy density and scanning method[28].



FigureA.2. Electron beam 3D printe

B-Ti6Al4V ALLOY

PURE TITANIUM. Pure titanium undergoes an allotropic transformation from the hexagonal close-packed alpha phase to the body-centered cubic beta phase at a temperature of 882.5°C . Alloying elements can act to stabilize either the alpha or beta phase. Through the use of alloying additions, the beta phase can be sufficiently stabilized to coexist with alpha at room temperature. This fact forms the basis for creation of titanium alloys that can be strengthened by heat treating. **TI6AL4V.** Titanium alloys are generally classified into three main categories: Alpha alloys, which contain neutral alloying elements (such as Sn) and/or alpha stabilizers (such as Al, O) only and are not heat treatable; Alpha + beta alloys, which generally contain a combination of alpha and beta stabilizers and are heat treatable to various degrees; and Beta alloys, which are metastable and contain sufficient beta stabilizers (such as Mo, V) to completely retain the beta phase upon quenching, and can be solution treated and aged to achieve significant increases in strength. Ti 6Al-4V is known as the "workhorse" of the titanium industry because it is by far the most common Ti alloy, accounting for more than 50% of total titanium usage. It is an alpha+beta alloy that is heat treatable to achieve moderate increases in strength. Ti 6Al-4V is recommended for use at service temperatures up to approximately 350°C (660°F). Ti 6Al-4V offers a combination of high strength, light weight, formability and corrosion resistance which have made it a world standard in aerospace applications[29].

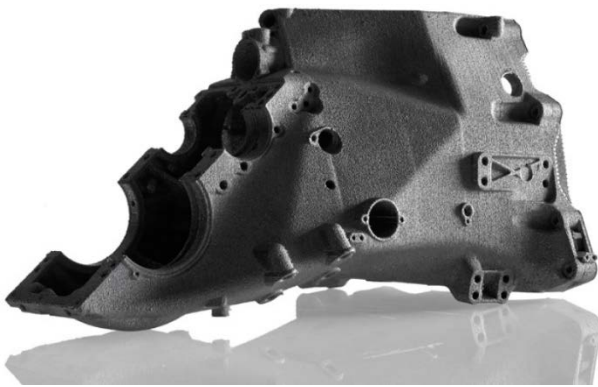


Figure B.1. Race car gear-box fabricated with Ti6Al4V

TI6AL4V SPECIFICS

Electrical Conductivity S/m	600000
Yield Strength MPa	950
Mass Density g/cm ³	4.41
Specific Heat J/Kg*°C	565
Thermal Conductivity W/m*°C	6.7
Young's Modulus Gpa	114
Poisson's Ratios	0.29

Table B. Ti6Al4V Specifics [30]

This page intentionally left blank

References

- [1] SLAC Linear Collider (SLC) <<http://www-sldnt.slac.stanford.edu/alr/slc.htm>>.
- [2] <http://clic-study.web.cern.ch/>
- [3] Linear Collider Detector CERN. <<http://lcd.web.cern.ch/LCD/>>.
- [4] Ellis, "New physics with the Compact Linear Collider". Nature 409, 431–435 (2001).
- [5] Delahaye, J.-P., Guignard, G., Raubenheimer, T. & Wilson, I. Scaling laws for e+/e-linear colliders. Nucl. Instr. and Meth. A 421, 369–405 (1998).
- [6] Schulte, D. in Proc. 8th European Particle Accelerator Conf., 3-7 June 2002, Paris, France (2002), 59–61. <<http://accelconf.web.cern.ch/AccelConf/e02/PAPERS/MOZGB002.pdf>>.
- [7] Delahaye, J.-P. in Proc. 1st Int. Particle Accelerator Conf., 23-28 May 2010, Kyoto, Japan (2010), 4769–4771. <<http://accelconf.web.cern.ch/accelconf/IPAC10/papers/frxcmh01.pdf>>.
- [8] Riddone, G., Schulte, D., Syratchev, I. & et al. in Proc. 11th European Particle Accelerator Conf., 23-27 June 2008, Genoa, Italy (2008), 607–609. <<http://accelconf.web.cern.ch/accelconf/e08/papers/mopp028.pdf>>.
- [8] A Multi-TeV linear collider based on CLIC technology: CLIC Conceptual Design Report, edited by M. Aicheler, P. Burrows, M. Draper, T. Garvey, P. Lebrun, K. Peach, N. Phinney, H. Schmickler, D. Schulte and N. Toge, 384-386. CERN-2012-007.
- [9] <http://www.ansys.com/Products/Workflow+Technology/ANSYS+Workbench+Platform/>
- [10] <http://www.ansys.com/Products/Simulation+Technology/Electronics/Signal+Integrity/ANSYS+HFSS>
- [11] Richard Feynman, "Feynman Lectures on Physics vol2". Caltech, Addison Wensley Longman, Ch.24,p1,2005.
- [12] Robert E. Collin, "Foundations for microwave engineering". New York, McGRAW-HILL ,97-102, 1992.
- [13] Southworth, G. C. "Electric Wave Guides" . Short Wave Craft, 198, 233. Retrieved March 27, 2015.
- [14] Robert E. Collin, "Foundations for microwave engineering". New York, McGRAW-HILL ,181-186, 1992.

- [15] N.Marcuvitz, 'Radiation Laboratory Series'. Massachusetts Institute of Technology, McGraw-Hill, 107-109, 1951.
- [16] CAS, 'CERN accelerator school RF engineering for particle accelerators'. Exeter College, Oxford, UK, S.Turner, 126-129, 1991.
- [17] F.Peauger et al., 'High Power Evaluation of X-band High Power Loads'; LINAC10, Tsukuba, p.226, September 2010
- [18] <http://www.microtech-inc.com/Products/WR-90-Waveguide-Flexible-Rectangular/p2s8/>
- [19] <http://octave.sourceforge.net/>
- [20] S.Federmann, F.Caspers, A.Grudiev, E.Montesinos, I.SYratchev, 'High Temperature Radio Frequency Loads', IPAC2011, San Sebastian (Spain), p.1, 2011.
- [21] S.H. Hall, S.G. Pytel, P.G. Huray, D. Hua, A. Moonshiram, G. Brist, and E. Sijercic, 'Multi-GHz, Causal Transmission Line Modeling Methodology with a Hemispherical Surface Roughness Approach', IEEE Transactions on Microwave Theory and Techniques, pp 2614 – 2624, December 2007.
- [22] M.Heretis, P.Spanoudakis, N.Tsourveloudis, 'Surface Roughness characteristics of Ti6Al4V alloy in conventional lathe and mill machining', Technical University of Crete, p.5 2009
- [23] <https://www.cst.com/Products/CSTMWS>
- [24] <http://www.3ds.com/products-services/catia/>
- [25] A.Grudiev, private communication
- [26] A.Grudiev, private communication
- [27] W.Wuensch, 'Clic accelerating structure development', Proceedings of EPAC, Genoa, p.4, 2008
- [28] P.Pearce, 'Klystron Modulators for the 3 TeV CLIC scheme', CERN, Geneva.
- [29] Halliday, Resnick, Krane 'Fundamentals of Physics', John Wiley and Sons, New York, Ch.6 pp.36-38, 2005.
- [30] Mc Naught, A. Wilkinson, 'Compendium of Chemical Terminology', Blackwell Scientific Publications, Oxford 1997
- [31] 'Forced Heat Convection', California state University, 2007. <http://www.csun.edu/~lcaretto/me375/07forced%20convection%20one.pdf>.
- [32] 'Forced Heat Convection', California state University, 2007. <http://www.csun.edu/~lcaretto/me375/07forced%20convection%20one.pdf>
- [33] A.Grudiev, private conversation
- [34] Flinn, Richard A.; Trojan, Paul K., 'Engineering Materials and their Applications'. Boston: Houghton Mifflin Company. p. 61, 1975.

[35] Incropera, Dewitt, Bergman, Lavine "Fundamentals of Heat and Mass Transfer", John Wiley & Sons, New York, pp.522-524, 2011.

[36] https://en.wikipedia.org/wiki/Selective_laser_sintering

[37] Prasad K. D. V. Yarlagadda; S. Narayana, "1st International Conference on Manufacturing and Management". Alpha Science p. 73-. ISBN 978-81-7319-677-5, 2011

[38] "How Selective Laser Sintering Works". THRE3D.com, 2014.

[39] ASTM International, ASTM F2792-12a, <http://www.astm.org/Standards/F2792.htm>

[40] "Electron Beam Melting". Thre3d.com, 2014.

[41] https://en.wikipedia.org/wiki/Electron_beam_additive_manufacturing

[42] <http://cartech.ides.com/datasheet.aspx?i=101&E=269>

[43] <http://www.arcam.com/wp-content/uploads/Arcam-Ti6Al4V-Titanium-Alloy.pdf>

Acknowledgement

I wish to thank Alexej Grudiev for being an example of integrity and correctness and for helping me during my stay at CERN.

I wish to thank Giovanni Marsella that has always been a resource of brilliant ideas.

I wish to thank Walter Wuensch for helping me integrating in my CERN group.

I wish to thank my family,

My father for being a good man,

My mother for being a good woman,

My sisters for being such lovely people.

I wish to thank my friends: Laura, Cindy and Francesca for helping me through my studies.

Finally, I wish to thank the woman I love for the memories she gives me.